1-1-2016

Regulation Of Cytochrome C Functions By Phosphorylation

Gargi Mahapatra
Wayne State University,

REGULATION OF CYTOCHROME *c* FUNCTIONS BY PHOSPHORYLATION

by

GARGI MAHAPATRA

DISSERTATION

Submitted to the Graduate School

of Wayne State University,

Detroit, Michigan

in partial fulfillment of the requirements

for the degree of

DOCTOR OF PHILOSOPHY

2016

MAJOR: BIOCHEMISTRY AND MOLECULAR BIOLOGY

Approved By:

_____

Advisor Date

_____

_____

_____

DEDICATION

This work is dedicated to my mother Pratima Mahapatra, father Pannalal Mahapatra, sister Nivedita Mahapatra, and my friend Rashmi Chandra, who encouraged me to be the best scientist I can be. The love and support of my family and friends kept me strong during my time while I conducted my PhD, and will help me to keep going for many years to come.

ACKNOWLEDGEMENTS

First and foremost, I would like to thank my advisor, Dr. Maik Hüttemann. Maik has been extremely understanding and supportive, guiding me on my journey, and providing the right balance of encouragement and constructive criticism, and most importantly, teaching me how to think forward and design experiments. I am grateful to my committee; Dr. Brian Edwards, Dr. Timothy Stemmler, and Dr. Miriam Greenberg. They have been understanding, insightful, flexible, have offered their valuable time, and have been a pleasant experience in graduate school. None of this would be possible without the Department of Biochemistry and Molecular Biology, and Center for Molecular Medicine and Genetics, namely the chairs, Dr. Bharati Mitra and Dr. Lawrence Grossman, the secretaries April Wolak and Suzanne Shaw, and financial administrator, Joseph Fiore. I would also take this opportunity to thank Dr. Siddhesh Aras for all the help, advice, and guidance that he offered. I must also thank all my friends, who made this journey so much more enjoyable.

I am eternally grateful for all the support of my previous and present colleagues, namely, Dr. Icksoo Lee, Jenney Liu, and Chistopher Sinkler for their friendly advice, for helping me with several assays related to the project, and the good times we shared. I would also like to thank Ms. Asmita Vaishnav for helping me with French Cell Press and protein purification from bacteria.

Last but not least, I thank my family for their unconditional love and encouraging words without which none of this would have been possible. Finally, I would like to thank all my collaborators who helped me in various aspects of my research by providing constructive conversations and/or reagents and raw materials.

TABLE OF CONTENTS

LIST OF FIGURES

LIST OF TABLES

CHAPTER 1 INTRODUCTION

1.1 Summary

The long term goal of my thesis research is to understand how tissue-specific phosphorylations on the small mitochondrial protein, cytochrome *c* (Cyt*c*), regulate its functions, under both physiologically healthy and stressed conditions, and to identify the cell signaling pathways targeting Cyt*c*. Cyt*c* is a functionally diverse protein that carries electrons in the electron transport chain and plays a critical role in cellular apoptosis, two diverse pathways that maintain cellular health that are active under diverse conditions. Since Cyt*c* plays a pivotal role in both these highly divergent pathways, regulation of the protein is very important—phosphorylation of the protein under physiological conditions hence implies a regulation by cell signaling pathways that have yet to be identified and studied. Previous work by our lab suggests the importance of reversible phosphorylation of Cyt*c* in regulating its functions [1-4]. We hypothesize that under healthy conditions, phosphorylated Cyt*c* partially inhibits mitochondrial respiration and maintains healthy mitochondrial membrane potential, preventing ROS generation, while cellular stress-mediated dephosphorylation leads to increased respiration and ROS generation, initiating apoptosis. To further test this hypothesis and to extend our understanding of Cyt*c* phosphorylation on its functions, I conducted two studies. In the first study, I investigated the physiological phosphorylation status of Cyt*c* in mammalian kidney tissues. To begin with, I purified bovine kidney Cyt*c* in the presence of phosphatase inhibitors, identified threonine phosphorylation by immunoblot analysis, and determined threonine 28 phosphorylation by immobilized metal affinity chromatography/nano-liquid chromatography/electrospray ionization mass spectrometry (Nano/LC/ESI/MS/MS). To

characterize the effect of Thr28 phosphorylation on Cyt*c* functions, I mutated Thr28 to glutamate, a phosphomimetic mutation, and alanine, a nonphosphorylatable control. I went on to express and purify wild-type, the phosphomimetic mutant and the non-phosphorylatable mutant Cyt*c* in bacterial cells. I also expressed and analyzed wild-type, the phosphomimetic mutant and the nonphosphorylatable mutant Cyt*c* in mammalian cells to determine the effects of the Cyt*c* mutations on the functions of the protein *in vitro* and on overall cellular metabolism and physiology, under healthy and stressed conditions. I also found that Thr28 phosphorylation is AMP kinase-mediated, and AMP kinase colocalizes with Cyt*c* to the mitochondrial intermembrane space. Our data suggest that Thr28, conserved in mammalian Cyt*c*, is an important regulatory site that leads to regulation of ETC flux via 'controlled respiration,' preventing $\Delta\Psi_m$ hyperpolarization, a known cause of ROS and trigger of apoptosis (discussed in Chapter 2, manuscript under preparation). In the second study, the phosphorylation status of Cyt*c* in ischemic brain was investigated to determine if insulin-induced neuroprotection and inhibition of Cyt*c* release in ischemic brain was associated with Cyt*c* phosphorylation. We used an animal model of global brain ischemia, and found a 50% decreased death rate of CA1 hippocampal neurons after neuroprotective post-ischemic insulin administration as compared to untreated controls. The increased survival of CA1 neurons was correlated to inhibition of Cyt*c* release from mitochondria into cytosol 24 hours post reperfusion, which in turn was mediated by Cyt*c* phosphorylation on Tyr97. We thus propose that Cyt*c* is phosphorylated by an insulin-dependent signaling pathway, and this may impede with its release from mitochondria and its ability to induce apoptosis (discussed in Chapter 3, manuscript published in PLoS One, 2013 8(11):e78627).

1.2 Cytochrome *c*

Cyt*c* is a small, 12.4 kDa globular protein localized in the mitochondrial intermembrane space under healthy or unstressed condition. It is a hemoprotein, with the heme group covalently linked to cysteines 14 and 17 of the peptide chain via thio-ether bonds. The hexa-coordinated, low-spin iron in the heme group is coordinated by His18 and Met80 residues. The human Cyt*c* protein is encoded by the nuclear gene, *CYCS*. [1][2] Being a nuclear-encoded gene, Cyt*c* is translated in the cytoplasm as apo-cytochrome *c*. The heme group is attached to apo-cytochrome *c* upon its translocation to the mitochondria. Under normal (i.e., non-apoptotic) conditions Cyt*c* is located in the intermembrane space of mitochondria, and is mostly associated with the outer surface of the inner mitochondrial membrane by electrostatic and hydrophobic interactions with the negatively charged phospholipids, in particular cardiolipin[5].

Cyt*c* is classified to the family of proteins containing covalently linked *c*-type cytochromes. Unlike other cytochromes, it is a positively charged, highly water-soluble protein, with a solubility approximately 100 g/L[6]. It is highly conserved across all species, with its presence in plants, animals, and several unicellular organisms. With only a few residues varying in mammals, it contains a highly conserved amino acid sequence. The high level of conservation makes it an extensively studied protein over the years, providing an insight into evolutionary biology. Studies of cytochrome c sequences revealed that sequences from humans and chimpanzees, our closest relative, were identical, whereas it was different from horses by 10 residues[7].

Cytochrome *c* is an essential protein in the electron transport chain between the quinol:cytochrome *c* oxidoreductase (complex III, or cytochrome bc1) and the

cytochrome *c* oxidase (complex IV, C*c*O or cytochrome a/a3), where it is involved in the generation of energy in the form of ATP. It is also one of the major players in intrinsic mitochondrial apoptosis. Cyt*c* can undergo oxidation and reduction, but it does not bind oxygen. This feature is utilized in the oxidative phosphorylation process, where Cyt*c* accepts a single electron from coenzyme Q – cytochrome *c* reductase and donates it to cytochrome *c* oxidase, the final electron acceptor that converts molecular oxygen to water. The latter is the proposed rate limiting step of the ETC[7]. While its function as an electron carrier is revealed under healthy cellular conditions, under stressed conditions, cytochrome *c* unveils its role in the intrinsic mitochondrial apoptosis cascade, by being released from the mitochondrial intermembrane space into the cytosol.

1.3 History of Cytochrome *c*

Microspectroscopic studies by C. S. McMunn (1852-1911) on tissue specimens across various phylum, from coelenterates to man, lead to the origination of the idea that heme proteins play a role in respiration. McMunn carefully removed blood from each sample and found a pigment that displayed a common absorption spectrum, thereby discovering cytochrome *c* in 1884. He termed the pigment myohaematin (in muscles) and histohaematin (in other tissues). He demonstrated intensification of bands by reduction and weakening by oxidation. Thus, he discovered a protein capable of redox functions in vertebrates and invertebrate, and showed that the chemistry of energy production in the body took place deep in the cellular structure of the tissues, and not just in the blood as had been previously assumed. These respiratory pigments are now known as cytochromes, and are fundamental to energy metabolism.

David Keilin, a Polish parasitologist in Cambridge, rediscovered cytochromes in 1925, and recognised MacMunn's achievement by identifying their function in cellular respiration [8]. Keilin's studies identified the same absorption bands identified by MacMunn not only in the fly, but in *Bacillus subtilis* and in baker's yeast. Keilin christened the ubiquitous colored pigments cytochromes. Cytochromes were further classified by Keilin by their lowest energy absorption band under reducing condition, naming them cytochrome *a* (604nm), *b* (564nm) and *c* (550nm)[8]. Keilin laid out the basic picture of the respiratory chain in the 1920's. Due to the presence of an iron (Fe) atom in heme it was believed that cytochrome *c* could act as an electron carrier by undergoing oxidation reduction reactions.

1.4 Structure of cytochrome *c*

Horse heart Cyt*c* was one of the first proteins to be crystallized. The *c*-type cytochromes, among the best studied players in mitochondrial electron transport, contain redox-active heme proteins for which X-ray crystallographic structures of Cyt*c* revealed that the heme group is covalently linked to the mature peptide chain of the protein (note that the mature protein lacks the N-terminal methionine residue) by two thioether bonds between the heme vinyls and cysteine residues 14 and 17 of the conserved heme-binding motif on the protein[9,10]. The heme iron exists in a hexacoordinate configuration with the His18 and Met80 residues acting as ligands. The heme iron-Met80 bond results in a weak 695 nm absorption band in the spectrum of oxidized Cyt*c*, the lack of which indicates that the protein is not correctly folded (Dickerson and Timkovich, 1975). Surrounded by aliphatic and aromatic side chains, the heme group resides in a very hydrophobic environment and this, together with the iron ligands His18 and Met80, provides an

explanation for the high redox potential of Cyt*c* (~260 mV in mammals) [4]. Only 7.5% of the heme surface remains exposed to the solvent [10], and it is this site that is used to transfer electrons from complex III to complex IV [11-14].

1.5 Cytochrome *c* is an essential protein

Murine embryos that are lacking Cyt*c* die in utero by midgestation[15]. They show a clearly evident and profound developmental delay at E8.5 and do not survive after stage E10.5. However, cell lines established from early Cyt*c* null embryos are viable under conditions that compensate for defective oxidative phosphorylation, and they are resistant to apoptosis via stimuli such as UV irradiation, serum starvation and staurosporine[15], and show reduced caspase-3 activity, but are highly sensitive to TNFα mediated cell-death signals[16,17]. This is because the intrinsic Cyt*c*-dependent apoptotic pathway remains inactive, while the extrinsic apoptotic pathway remains active. Since the primary role of Cyt*c* is to carry electrons in the ETC, Cyt*c* null cells suffer from a defective electron transport and oxidative phosphorylation system, leading to early lethality of the embryos.

1.6 Functions of cytochrome *c*:

1.6.1 Role of cytochrome *c* in oxidative phosphorylation

Cyt*c* is located in the mitochondrial intermembrane space, and in the terminal step of the ETC, reduced Cyt*c* carries a single electron from complex III to complex IV (cytochrome *c* oxidase), which in turn oxidizes Cyt*c* and reduces a single molecule of oxygen to water on transfer of four such electrons. Under physiological conditions in intact mitochondria, this is the rate-limiting step of the ETC [18-22]. The irreversible conversion of oxygen to water is accompanied by a free energy change of $\Delta G^{o'} = -100$ kJ/mol [23].

1.6.2 Cytochrome *c* and Erv1-Mia40-coupled protein import

Cyt*c* is synthesized from its nuclear gene as apocytochrome *c*, imported into mitochondrial intermembrane space and is converted into the holo-form by the Cyt*c* heme lyase-catalyzed heme addition [24]. In the intermembrane space, it functions in the redox-coupled protein import pathway along with the transporters of outer membrane (TOMs), Erv1, and Mia40 proteins. Together, they import small transporters of inner membrane (TIMs) and other proteins that contain the twin CX3C and CX9C motifs into the intermembrane space [25]. Then, these proteins undergo post-import modifications such as alternative folding, and on being oxidized by Mia40, these proteins form disulfide bonds between the cysteine residues that finally lock alter their tertiary structure [26]. Mia40 is reactivated by Erv1-mediated oxidation, and Erv1 is reoxidized by Cyt*c* [27]. The electrons that are sequentially transported from the imported protein to Mia40 to Erv1 to Cyt*c* finally feed into the ETC.

1.6.3 Role of cytochrome *c* as both a ROS scavenger and producer

A) During the transfer of electrons by the ETC complexes, redox intermediates are generated mainly by complexes I and III and the reduced ubiquinol pool. These intermediates can also take part in various side reactions and as a result, transfer electrons directly to oxygen, generating ROS as a byproduct of the ETC [28,29]. The cells are equipped with radical scavenging enzymes to neutralize ROS, such as superoxide dismutase (SOD) and catalase. Cyt*c* is constantly reduced by complex III and oxidized by complex IV, and is thus capable of performing the functions of an antioxidant. Along with SODs and catalase, Cyt*c* also removes unpaired electrons from superoxides generated in the intermembrane space, regenerating O_2 [30,31], finally donating these electrons to cytochrome *c* oxidase (COX). It also scavenges hydrogen peroxides [32].

B) A splice variant of the growth factor adapter Shc, namely p66shc, is found throughout the cell with a subset localizing to the mitochondria, where it affects mitochondrial function [33]. Under stress conditions, mitochondrial p66shc is oxidized by electrons supplied by Cyt*c*, which leads to the p66shc-mediated production of hydrogen peroxide [34]. The increase in ROS production via p66shc as part of the apoptotic pathway would provide Cyt*c* with peroxide equivalents necessary for the oxidation of cardiolipin, a process that is required for its release from the mitochondria as discussed below. Indeed, release of Cyt*c* correlates with the H_2O_2 production activity of p66shc [35], and could be a significant switch utilized by the cell as an initiating event of apoptosis.

1.6.4 Role of cytochrome *c* in apoptosis

Cyt*c* plays an essential function in the induction of apoptosis, as was established more than a decade ago [36], and it is not degraded during apoptosis [37]. Thousands of studies have furthered this knowledge and now, the established model of mitochondrial type II apoptosis considers Cyt*c* release from mitochondria into the cytosol and binding to apoptotic protease-activating factor 1 (Apaf-1) as a key committing steps [38]. The essentiality of Cyt*c* for apoptosis is further strengthened by the fact that Cyt*c* null cell lines show reduced caspase-3 activation after stimulation of apoptosis [15], along with a decreased rate of ATP production. Previous work also indicates that Cyt*c* can be reversibly released and taken up by isolated mitochondria [39], and membrane rupture or mitochondrial permeability transition pore opening are not always necessary for the execution of apoptosis [40]. However, before the point of no return is reached, a certain proportion of Cyt*c* must be released from the mitochondria [41].

1.6.5 Cytochrome *c*-catalyzed cardiolipin oxidation precedes cytochrome *c* release

Cardiolipin is a mitochondria-specific lipid and mainly localized in the inner mitochondrial membrane where it binds ~15-20% of Cyt*c* [42,43]. During apoptosis, Cyt*c* functions as a cardiolipin peroxidase [44], and this oxidation decreases the affinity of Cyt*c* for cardiolipin [44,45], thereby increasing the amount of free Cyt*c* in the intermembrane space, which can then be released into the cytosol once the mitochondrial outer membrane is ruptured. This peroxidase function of Cyt*c* depends on the physical interaction between Cyt*c* and cardiolipin and involves a tyrosine radical [44,46,47].

1.7 Cytochrome *c* regulation:

Being at the crux of the ETC, the terminal rate-limiting step of the ETC is regulated by various means, as described hereunder.

1.7.1 Allosteric regulation

Both Cyt*c* and COX are regulated allosterically by the ATP/ADP ratio. ATP binds to Cyt*c* and to COX, acting as an allosteric inhibitor [48-50]. The structure and electrostatic properties of both the proteins are presumed to be changed upon ATP binding, which decreases the capability of Cyt*c* to transfer electrons [51,52], thereby downregulating ETC flux when there is already a high level of ATP within the cell.

1.7.2 Regulation via expression of tissue-specific isoforms

Another mode of regulation commonly seen in the ETC proteins is via tissue-specific isoform expression. A testis-specific isoform of Cyt*c* (T-Cyt*c*) exists in germinal epithelial cells of rodents [53], having 86% homology with the amino acid sequence of somatic Cyt*c* (S-Cyt*c*), and is the predominant form of Cyt*c* in mature sperm [53-55]. T-Cyt*c* shows three-fold higher H_2O_2 reduction rates and about four-fold higher apoptotic activity [55]. However, this isoform is not evolutionarily conserved, and exists as a pseudogene in

humans [7,56]. Human Cyt*c*, which is ubiquitously expressed including in testis, shows 91% homology to mouse Cyt*c*-S and 82% homology to Cyt*c*-T.

1.7.3 Regulation by post-translational modifications

The third mode of Cyt*c* regulation is by post-translational modifications. The overall working hypothesis in our lab is that in higher organisms, the main mode regulating energy production is through cell signaling pathways triggered by various extracellular cues. Cyt*c* has been found to be trimethylated at evolutionarily conserved residue Lys77 in *S. cerevisiae* and plants [57-60]. Also established is the role of Lys72-methylation in determining the pro-apoptotic activity of Cyt*c* [61]. Lys77-trimethylation was suggested to be important for protection of Cyt*c* from proteolytic cleavage, and abrogation of proapoptotic activity. In addition, Cyt*c* nitrosylation on its heme iron during apoptosis has been suggested to increase the protein's proapoptotic function [62].

1.7.3.1 Regulation by reversible phosphorylations

Over 400 phosphorylation sites have been mapped on the oxidative phosphorylation complexes from various species to date [63], and a few recent studies indicate that several kinases and phosphatases are present in the mitochondria or that they can translocate into the mitochondria after stimulation of signaling pathways as was shown for the EGF receptor [64]. However, of the sites mapped, only a handful have been functionally studied (mainly by our group), while the kinases and phosphatase involved in these phosphorylations remain elusive for essentially all mapped sites. In mammals, 18 phosphorylation sites have been mapped on COX and 4 on Cyt*c* [65,66].

The recent discovery of *in vivo* tyrosine phosphorylation of mammalian Cyt*c* by our lab has helped in our understanding of how kinases and phosphatases differentially

modify Cyt*c* functions during different cellular conditions. Cyt*c* was previously isolated by our lab in the presence of the nonspecific phosphatase inhibitors fluoride and vanadate to maintain phosphorylations, and has been found to be phosphorylated on two different highly conserved tyrosine residues by mass spectrometry, namely Tyr97 and Tyr48 in heart and liver tissues, respectively [1,67]. This indicates that cell signaling pathways target the protein in a tissue-specific manner. As discussed above, oxidized Cyt*c* exhibits a specific absorption band at 695 nm due to a bond between a Met80 residue and the heme iron, a signal called the "indicator of trouble", which is lost when the protein is either denatured or dysfunctional (Dickerson and Timkovich, 1975). Tyr97-phosphorylated Cyt*c* showed a shift in this band from 695 nm to 687 nm, suggesting an effect on the heme environment [1]. Both phosphorylations also had a direct effect on the various functions of Cyt*c*. For example, both tyrosine phosphorylations resulted in decreased, partially inhibited oxygen consumption in the reaction with isolated COX *in vitro*, with Tyr97-phosphorylated Cyt*c* showing sigmoidal kinetics, while Tyr48-phosphorylated Cyt*c* showed hyperbolic kinetics, similar to alkaline phosphatase-treated unphosphorylated Cyt*c* [1,67]. Tyr48 phosphorylation has been studied in detail by creating a Tyr48Glu phospho-mimetic mutant, and was shown to completely abolish activation of caspase3 *in vitro* [68]. This suggests that Tyr48-phosphorylation might be an important regulator of the protein's function as an initiator of mitochondrial type II apoptosis. In the cellular context, this regulation might be occurring through a phosphorylation-mediated change in conformation of the native protein that changes the interaction between Cyt*c* and Apaf1 in the cytosol, and results in impaired apoptosome formation. Lys7 is one residue that is

important for this interaction [69], and being spatially located right next to Tyr97, might be regulated by phosphorylation of that site.

In addition to Cyt*c*, COX subunits have also been found to be phosphorylated at various sites by different pathways, including protein kinase C signaling, receptor tyrosine kinase, and inflammatory signaling through the TNFα signaling pathway. It was seen that after *in vitro* dephosphorylation of cow liver COX, the inhibitory effect of ATP on COX was lost [70]. This finding rationalizes studies of allosteric regulation of phosphorylated Cyt*c* and COX by ATP.

1.7.3.2 Regulation of Cyt*c* by site-specific phosphorylations, in mammalian kidneys and brain under physiologically healthy and stressed conditions

To continue my research on extending our knowledge and understanding of how phosphorylation of Cyt*c* affect its functions under healthy and stressed conditions, I chose to work with tissues that are physiologically different than heart and liver tissues. In Chapter 2, I show that mammalian kidney Cyt*c* is phosphorylated at Thr28 under physiologically healthy conditions, a conserved site in mammalian Cyt*c*. My results suggest that Thr28 is an important regulatory site, involved mainly in maintaining optimal intermediate mitochondrial membrne potential ($\Delta\Psi_m$) levels, thereby regulating energy production and preventing ROS generation. Also, my results suggest that Thr28 phosphorylation of kidney Cyt*c* in the mitochondrial intermembrane space is mediated by AMPK, a metabolic sensor that was found to be basally active in kidney. In Chapter 3, we show that neuroprotective insulin treatment prior to brain ischemia/reperfusion results in phosphorylation of brain Cyt*c* on Tyr97, leading to decreased Cytc release from mitochondria into the cytosol, resulting in reduced death of neurons, and thus

neuroprotection. The data in Chapter 3 have been published [71]. Chapter 4, contains conclusions and future directions.

CHAPTER 2 AMPK-MEDIATED PHOSPHORYLATION OF CYTOCHROME *c* THREONINE 28 REGULATES ELECTRON TRANSPORT CHAIN ACTIVITY IN KIDNEY

2.1 Introduction

Cytochrome *c* (Cyt*c*) is a small (12 kD) globular nuclear-encoded mitochondrial protein containing a covalently attached heme group. It functions in the electron transport chain (ETC) as a single electron carrier between bc_1 complex (complex III) and cytochrome *c* oxidase (C*c*O, complex IV), and is thus essential for aerobic energy production. The second important role of Cyt*c* is seen under conditions of stress, when it functions as a crucial pro-apoptotic signal [72]. During apoptosis, Cyt*c* is released from mitochondria into the cytosol, where it interacts with Apaf-1 to form the apoptosome, which in turn activates caspase-9 and the downstream executioner caspase cascade. Furthermore, Cyt*c* functions as a cardiolipin peroxidase during the early phase of apoptosis, when it oxidizes the mitochondrial membrane lipid cardiolipin, thus facilitating its own release from the inner mitochondrial membrane. In contrast, under healthy, non-apoptotic conditions Cyt*c* acts as a scavenger of reactive oxygen species (ROS) [31], and it takes part in other redox reactions inside mitochondria including redox-coupled protein import [26] and reduction of p66Shc, a protein that is implicated in the generation of ROS, apoptosis, and in regulating lifespan [34]. Given the multiple functions of Cyt*c* it is not surprising that it is tightly regulated. Two regulatory mechanisms via expression of a somatic and testis-specific isoform pair and allosteric regulation through binding of ATP have been known for over 30 years [49,53]. A third mechanism via reversible phosphorylation was discovered recently when we purified bovine Cyt*c* from heart and liver tissue under conditions preserving the physiological phosphorylation status. The two proteins were phosphorylated respectively on Tyr97 and Tyr48 [73,74]. Both modifications

lead to a partial inhibition of respiration. In addition, the phosphomimetic Tyr48Glu substitution abolished the capability of Cyt*c* to trigger apoptosis, suggesting that Cyt*c* phosphorylation regulates apoptosis at the level of the apoptosome [75]. Here we report that Cyt*c* purified from bovine and rat kidney tissues in the presence of phosphatase inhibitors is phosphorylated on threonine 28 (Thr28). In vivo phosphorylated and Thr28Glu phosphomimetic Cyt*c* lead to an inhibition of respiration in the reaction with C*c*O. Introduction of wild-type (WT) and Thr28Glu phosphomimetic Cyt*c* into Cyt*c* knockout cells shows that intact cell respiration, mitochondrial membrane potential ($\Delta\Psi_m$), and ROS levels are reduced. This suggests that Cyt*c* phosphorylation can regulate ETC flux, preventing $\Delta\Psi_m$ hyperpolarization, a known trigger of ROS production and apoptosis [76]. Finally, we provide in vivo and in vitro evidence suggesting that phosphorylation of Thr28 is mediated by AMP kinase (AMPK), which co-localizes with Cyt*c* in the mitochondrial intermembrane space. This is the first report of a mapped phosphorylation site on a mammalian oxidative phosphorylation component, together with functional and structural analyses and a kinase candidate mediating this site-specific modification.

2.2 Materials and methods

2.2.1 Isolation of cytochrome *c* from bovine kidney tissue

Reagents and chemicals were purchased from Sigma unless stated otherwise. All procedures involving animal tissues were approved by the Wayne State University Institutional Animal Care and Use Committee. Kidneys from freshly slaughtered cows were snap frozen on dry ice, and stored at -80ºC until used for Cyt*c* purification by the acid-extraction method [74]. For a detailed protocol see Supplemental Information.

2.2.2 Western analyses

Western analyses were performed using the enhanced chemiluminescence method. See Supplemental Information for antibody details.

2.2.3 Mass spectrometry of purified cytochrome *c* to detect site-specific phosphorylation

Phosphorylation sites mapping on purified kidney Cyt*c* was performed after tryptic digestion and TiO_2 enrichment of phospho-peptides, following C18 reversed-phase chromatography as described [71]. Peptides were injected into the mass spectrometer (LTQ Orbitrap-Velos, Thermo Scientific, Waltham, MA) after electrospray ionization. MS/MS spectra were obtained in positive ion mode, assigned to peptide sequences from the UniProt protein database, searched with the MASCOT algorithm for PTMs, and manually verified.

2.2.4 Mutagenesis, expression, and purification of cytochrome *c* variants

Rodent somatic Cyt*c* cDNA was cloned into the pLW01 expression vector as described [75] and threonine 28 (Thr28) was mutated to the phosphomimetic glutamate and nonphosphorylatable alanine as an additional control by mutagenesis PCR. Constructs were transformed into competent *E. coli* C41 (DE3) cells for protein overexpression [75]. Cells were lysed using a French Pressure Cell Press and Cyt*c* variants were purified by ion exchange chromatography as described above for kidney Cyt*c* isolation. A similar mutagenesis was used for expression of Cyt*c* variants in Cyt*c* double knockout mouse lung fibroblasts using the pBABE-puro expression plasmid (Addgene, Cambridge, MA) following selection of stably expressing cell lines. Wild-type and Cyt*c* double knockout lung fibroblasts were previously characterized in detail [77]. See Supplemental Information for details.

2.2.5 Crystal structure determination

Briefly, using the PHENIX suite of programs [78], the structure of WT Cyt*c* was solved by molecular replacement using chain-A of human Y46F Cytc [79], refit automatically to the experimental electron density with PHENIX, and refined to obtain occupancy values for the FC6 ligands. The refinement was completed to an R-free of 0.159 at 1.12 Å resolution using REFMAC5 [80] with parameters optimized by PDB_REDO [81]. The WT structure (5C0Z.pdb) was then used to solve, refit, and refine the structures of the Thr28Ala (5C9M.pdb) and Thr28Glu (5DF5.pdb) mutants at 1.36 Å (Rfree: 0.170) and 1.30 Å (Rfree: 0.178) resolution, respectively. All proteins were oxidized with 5 mM $K_3Fe(CN)_6$ prior to crystallization. Full details and comparative statistics are provided in Supplemental Table 1.

2.2.6 Cytochrome *c* oxidase (C*c*O) activity measurements

C*c*O activity with Cyt*c* variants was determined using the polarographic method as described [82]. For a detailed protocol, see Supplemental Information.

2.2.7 Caspase 3 activation by cytochrome *c* variants

The capability of Cyt*c* purified from bovine kidneys and the bacterially expressed Cyt*c* mutants to induce downstream caspase 3 activity were assessed in vitro with cytoplasmic extracts of a mouse lung fibroblast cell line lacking both the somatic and testis-specific Cyt*c* genes [77] as described [75]. For a detailed protocol see Supplemental Information.

2.2.8 Measurement of Cyt*c* redox potential, heme degradation, and oxidation and reduction rates

The midpoint redox potential ($E^{0'}$) was analyzed spectrophotometrically as described [75]. The kinetics of oxidation of 15 µM ferro-Cyt*c* with 100 µM H_2O_2 and reduction

of 15 µM ferri-Cyt*c* with 200 µM ascorbate was measured spectrophotometrically at 550 nm, and heme degradation in the presence of 3 mM H_2O_2 was determined via dissipation of the 408 nm Soret band as described [55]. For detailed protocols see Supplemental Information.

2.2.9 Peroxidase activity of Cyt*c* mutants

Assessment of peroxidase activity [75] with Amplex Red reagent was performed by measuring the fluorescence of resorufin, an oxidation product of Amplex Red. Cyt*c* (1 µM) was incubated with liposomes containing TOCL/DOPC in ratio 1:1 for 10 min. Peroxidase reaction was started by addition of Amplex Red (50 µM) and H_2O_2 (50 µM) and was carried out for 20 min during which the reaction rate was linear. Fluorescence was detected by employing a "Fusion R" universal microplate analyzer by using an excitation wavelength of 535 nm and an emission wavelength of 585 nm.

2.2.10 In vitro phosphorylation of cytochrome *c* with AMP kinase

Cow heart Cyt*c* (300 pmoles; Sigma) was incubated with 3 pmoles of AMPK (AMPK α1/β1/γ1, Active SignalChem, P47-10H) at 37ºC for 5 or 30 min in the presence and absence of AMP (125 µM) in 25 mM MOPS (pH 7.2), 12.5 mM beta glycerophosphate, 25 mM $MgCl_2$, 2 mM EDTA, 0.25 mM DTT, and 1 mM ATP. Samples were analyzed by Western blot and mass spectrometry.

2.2.11 Immunoprecipitation and Western analyses from tissue homogenates

All Western analyses from tissue homogenates were done using 20 µg of whole tissue homogenates. All immunoprecipitations from tissue homogenates were done with 1 mg of tissue homogenate. For immunoprecipitations, 50 µL of bead (ImmunoCruz

IP/WB Optima E and F Systems: sc-45042 and sc-45043) and 5 µg antibody were allowed to conjugate overnight at 4ºC, centrifuged (22,000 x g) for 30 seconds and washed twice with 500 µL PBS. Immunoprecipitation was performed by addition of 1 mg tissue homogenate and rotation overnight at 4ºC.

2.2.12 Tissue Treatments with AMPK activator A-769662 and inhibitor Compound C

Fresh mouse kidneys were minced and treated with 500 µM A769662 (AMPK activator, Tocris, #3336) or 3 µM Compound C (AMPK inhibitor, Sigma, P5499) for 1 h following Western analysis of the soluble fraction. In addition, AMPK was immunoprecipitated from kidney homogenates after treatment with 500 µM A769662 for 1 h to analyze Cyt*c* co-immunoprecipitation. See Supplemental Information for details.

2.2.13 Measurement of mitochondrial oxygen consumption rate tissue homogenates

Respiration of intact mitochondria in tissue homogenates was determined as described [83]. For a detailed protocol see Supplemental Information.

2.2.14 Presence of AMP kinase in mitochondria and mitochondrial subfractionation

Mouse kidneys were freshly harvested and washed in ice-cold isolation buffer (10 mM Tris, 1 mM of EGTA/Tris, 200 mM sucrose, pH 7.4 adjusted with MOPS) [84], minced, and homogenized with 20 strokes using a dounce homogenizer on ice following mitochondria isolation by sucrose density gradient purification. The mitochondrial pellet was subfractionated into an intermembrane space fraction and a mitoplast and outer membrane fraction. For detailed protocols see Supplemental Information.

2.2.15 Measurement of oxygen consumption rate in intact cells

Per well, 70,000 cells were cultured in growth media (DMEM, supplemented with 10% FBS, 2% penicillin/streptomycin, 1 mM pyruvate and 50 µg/mL uridine) using

Seahorse XF^{e}24 plates. After overnight culture, growth media was replaced with XF media, pH 7.4, and intact cell respiration was measured.

2.2.16 Mitochondrial ROS measurement

Cells expressing Cyt*c* variants were cultured in 12 well plates and incubated with 5 µM Mitosox for 30 min in at 37ºC. Cells were washed with PBS and fluorescence analyzed with a Synergy H1 plate reader (BioTek, Winooski, VT) by using excitation and emission wavelengths of 510 nm and 590 nm.

2.2.17 ATP, mitochondrial membrane potential, and cell viability measurements

ATP levels were measured from lung fibroblast cells expressing Cyt*c* variants applying the bioluminescent method. Mitochondrial membrane potential ($\Delta\Psi_m$) and cell viability were measured with JC-1 (Molecular Probes) and tryphan blue staining, respectively. For detailed protocols see Supplemental Information.

2.2.18 Isolation of cytochrome *c* from bovine kidney tissue

All steps were performed at 4ºC or on ice. Kidney tissues were homogenized in 100 mM phosphate buffer, pH 4.5, adjusted with acetic acid, and incubated overnight at 4ºC. Under those conditions most cellular proteins denature and precipitate, whereas Cyt*c* is extracted and stays in solution. The homogenate was centrifuged at 15,810 x g for 35 min, supernatants decanted through cheesecloth, and pH adjusted to 7.4 with KOH, while simultaneously adding protease (10 mM PMSF) and phosphatase inhibitors (1 mM KF, 1 mM Na-orthovanadate), thus preserving the phosphorylation state of Cyt*c*. The supernatant was incubated at 4ºC for 20 min and centrifuged following ion exchange chromatography. First, the supernatant was passed through a DE52 anion exchange

column equilibrated with 20 mM phosphate buffer, pH 7.4, 3.6 mS/cm conductance. Cyt*c* was collected in the flow through, which was pH readjusted to 6.5 and applied to a CM52 cation exchange column equilibrated with 30 mM phosphate buffer, pH 6.5, 5.5 mS/cm conductance. Cyt*c* bound to the CM52 column was oxidized on the column with 2 mM $K_3Fe(CN)_6$, and was eluted by step gradient using 30, 50, 80, 120, and 150 mM phosphate buffers, pH 6.5. To obtain a highly pure fraction of Cyt*c*, the DE52 and CM52 ion exchange chromatography steps were repeated. For further purification HPLC size-exclusion chromatography, with a column equilibrated with 150 mM phosphate buffer, pH 6.5, was performed and a mixture of phosphorylated and nonphosphorylated Cyt*c* was obtained. The protein was concentrated under vacuum, desalted by centrifugation using Amicon Ultra-15 3kDa centrifugal filter units (Millipore, Billerca, MA), and stored at -80ºC.

2.2.19 Protein concentration and purity determination

Purified Cyt*c* was reduced with 100 mM sodium dithionite, desalted with NAP-5 columns (GE Healthcare, Piscataway, NJ), and analyzed on a Jasco V-570 double beam spectrophotometer (2 nm band width). The concentration was determined by differential spectra at 550 nm by subtracting the oxidized form from the reduced and calculated via $\varepsilon(\text{red.}-\text{ox.})_{550\ nm}=19.6\ mM^{-1}\ cm.^{-1}$ Purity of the protein was confirmed by Coomassie staining after 12% Tris-Tricine SDS PAGE.

2.2.20 Gel electrophoresis and Western blotting

Western analyses were performed to analyze the phosphorylation status of purified Cyt*c*, with a 1:5000 dilution of primary antibodies: anti-phospho tyrosine (4G10, Millipore, Bilerica, MA), anti-phosphoserine (set of four individual monoclonal antibodies,

1C8, 4A3, 4A9, and 16B4, EMD Biosciences, Gibbstown, NJ), and anti-phosphothreonine antibodies (set of three individual monoclonal antibodies, 1E11, 4D11, and 14B3, EMD Biosciences, Gibbstown, NJ) followed by a 1:10,000 dilution of anti-mouse IgG or IgM horseradish peroxidase conjugated secondary antibody (GE Healthcare). EGF-stimulated A431 total cell lysate (Upstate, Bilerica, MA) was used as a positive control and ovalbumin as a negative control. Signal detection was performed with an enhanced chemiluminescence method (GE Healthcare, Piscataway, NJ). The following antibodies were used at a dilution of 1:1,000: complex I NDUFB6 (MS108, MitoSciences, Eugene, OR); complex II 70kD subunit (MS204, MitoSciences, Eugene, OR); complex III core I (MS303, MitoSciences, Eugene, OR); complex IV Subunit I (MS404; MitoSciences, Eugene, OR); complex IV subunit IV (sc58348, Santa Cruz Biotechnology, Dallas, TX); cytochrome *c* (556433, BD Pharmingen, San Jose, CA); porin (MSA03, MitoSciences, Eugene, OR); and GAPDH: (ab9484, Abcam). To separate Thr28-phosphorylated from unphosphoryated Cyt*c* a 15% acrylamide/2.6% bisacrylamide gel (Tris-tricine-SDS PAGE) was prepared. Cyt*c* (500 ng) was denatured in 2x sample buffer (NuPAGE, NP0007, Invitrogen) with 100 mM DTT and 3% mercaptoehanol. Anode and cathode buffers were 0.2 M Tris pH, 8.9 and 100 mM Tris, 100 mM Tricine, 0.1% SDS, pH 8.25) and gels were run at a low voltage (80 V) for up to 4 h.

2.2.21 Mutagenesis, expression, and purification of cytochrome *c* variants

Mouse somatic Cyt*c* cDNA was cloned into the pLW01 expression vector (kind gift from Dr. Lucy Waskell, University of Michigan) that also contained the cDNA encoding heme lyase (CYC3), an enzyme necessary for the covalent attachment of the heme group to apo-Cyt*c*. Threonine 28 (Thr28) in the wild type Cyt*c* cDNA was mutated to the

phosphomimetic glutamate and nonphosphorylatable alanine as an additional control. Forward primers 5'-AAGCATAAGGAGGGACCAAA-3' (T_m=53.8°C) and 5'-AAGCATAAGGCTGGACCAAA-3' (T_m=53.8°C) and corresponding reverse and complement primers 5'-TTTGGTCCCTCCTTATGCTT-3' (T_m=54.6°C) and 5'-TTTGGTCCAGCCTTATGCTT-3' (T_m=54.6°C) were used for Thr28Glu and Thr28Ala mutagenesis PCR, respectively. The outer primers that amplified the entire Cyt*c* cDNA sequence containing NcoI and BamHI restriction sites were 5'-AATTTACCATGGGTGATGTTGAAAAAG-3' (T_m=56.7°C) and 5'-AATAAAGGATCCAGTGGAATTATTCAT-3' (T_m=54.7°C), respectively. The mutated Cyt*c* cDNA sequences were subcloned into the pLW01 bacterial expression plasmid after restriction digestion with NcoI and BamHI. Note that the Cyt*c* cDNA contains an internal NcoI restriction site; thus the fragments were first fully digested with BamHI following partial (3 min) digestion with NcoI and purification of the correct size fragment after agarose gel electrophoresis. Constructs were confirmed by sequencing and used to transform competent *E. coli* C41 (DE3) cells for protein overexpression [75]. The clones were inoculated into 20 mL TB medium (Difco, BD, Franklin Lakes, NJ) containing 100 µg/mL carbenicillin and grown overnight at 37ºC under shaking. These cultures were used to inoculate 4 L of 100 µg/mL carbenicillin-containing TB medium and were grown until an OD_{600} of 2-3 was reached. At this time, the expression of cytochrome *c* was induced by addition of 100 mM isopropyl β-D-1-thiogalactopyranoside (IPTG), and the protein was overexpressed for 6 h at 37ºC. The cells were harvested by centrifugation for 40 min at 8,400 x g, 4ºC, and the pellets were immediately stored at -80ºC until used for Cyt*c* extraction. The bacterial pellets were resuspended in lysis buffer containing 20 mM

phosphate buffer, pH 7.4 supplemented with a protease inhibitor cocktail (P8340, Sigma) as recommended by the manufacturer. For every 10 g of bacterial pellet 100 ml of lysis buffer were used and the resuspended cells were lysed using a French Pressure Cell Press (American Company, Aminco). The lysates were centrifuged at 15,000 rpm for 45 min, the pH of the supernatant was adjusted to 7.4 and Cyt*c* variants were purified by ion exchange chromatography as described above for kidney Cyt*c* isolation. For expression of Cyt*c* variants in Cyt*c* double knockout mouse lung fibroblasts the pBABE-puro expression plasmid (Addgene, Cambridge, MA) was used. A similar PCR mutagenesis approach was performed as above and fragments were cloned into the BamHI and EcoRI restriction sites using the primers outer forward primer pBABE 5'-ATCTTGTGGAAAGGACGCGGGATCCATGGGTGATGTTGAAAAA-3' (T_m=68.0°C) and outer reverse primer pBABE 5'-GGTCGACCACTGTGCTGGCGAATTCTTACTTATCGTCGTCATCCTTGTAATCTTCATTAGTAGCC-3' (T_m=68.8°C). The resultant C-terminal 1XFLAG-tagged wild-type, Thr28Glu phosphomimetic mutant, and Thr28Ala non-phosphorylatable mutant constructs were transfected into Cyt*c* double knockout lung fibroblast cells and cultured in DMEM media (high glucose, Gibco BRL), supplemented with 10% fetal bovine serum, 1000 units penicillin/streptomycin, 1mM pyruvate, 50 μg/mL uridine at 37°C and 5% CO_2. Stable cell lines expressing the three Cyt*c* variants as well as an empty vector control cell line were selected in the presence of 4 μg/mL puromycin.

2.2.22 Circular dichroism spectroscopy

Circular dichroism (CD) spectra of cytochrome *c* variants (wild type, Thr28Ala, Thr28Glu, and bovine heart cytochrome *c* (Sigma)) were recorded on a Jasco J-815

spectrometer using a 0.6 mm path length quartz cuvette. Proteins were diluted to 220 μM final concentration in 100 mM phosphate buffer, pH 7.4, and 1 mL protein solution was reduced with 250 μM ascorbate. An average of 3 scans were collected at 20°C at a resolution of 1 nm.

2.2.23 Crystallization of WT, T28A, and T28E cytochrome *c*, and data analysis

Cyt*c* was gel-filtered on a S100 column to reduce aggregates and concentrated to 15 mg/mL or higher in water. To establish a defined oxidation state, the proteins were oxidized with 5 mM $K_3Fe(CN)_6$ prior to crystallization. Crystals were grown by vapor diffusion after mixing 1 μL of protein solution with 1μL of precipitant solution and equilibrating the drop against 0.5 mL of the precipitant at room temperature. The respective precipitant solutions for crystals of the WT, T28A, and T28E Cyt*c* are listed in Supplemental Table 1. Crystals usually appeared within 1 week. Crystals were soaked for 10 minutes in a cryo-protectant solution (Supplemental Table 1) before flash freezing in liquid nitrogen. Single crystal diffraction data were collected at the Life Sciences Collaborative Access Team facility (Advanced Photon Source sector 21, Argonne National Laboratory). The data were collected over a full 360° rotation in either 0.6 or 1.0 degree frames and integrated using XDS [85] in AutoProc [86]. For structure solution and refinement the native data set was solved using chain-A of the human Y48F Cyt*c* structure (3ZOO.pdb) in PHENIX [78]. It was refit with AutoBuild in the PHENIX suite and refined with PHENIX initially to get occupancies for the FC6 molecules. The refinement was completed with Refmac5 in CCP4 using refinement parameters and weights optimized with PDB_REDO. In particular, PDB_REDO recommended anisotropic temperature factors based on the Hamilton ratio test for all three structures. Electron density was

analyzed with COOT [87] in the CCP4 suite of crystallographic programs [88]. The FC6 ligands were located and placed in an anomalous diffraction difference map with COOT. Using the WT structure as an example, the highest 8 peaks - in order - in the map, are the 4 heme iron atoms, followed by FC6 202/C, FC6 202/B, FC6 202b/A, and FC6 203b/B. The next 3 peaks are for three sulfur atoms (Cys14/A, Cys17/B, Met80/D) followed by FC6 202a/A and FC6 202a/B. The last two FC6 positions were included because they had sufficient 2Fo-Fc density to fit several of their cyanide groups.

2.2.24 Molecular dynamics and ESP calculations

Molecular dynamics were performed with YASARA [89] using its conservative "slow" protocol and the recommended default force field, AMBER 2003 [90]. The Root Mean Square Fluctuations (RMSF) and average structures plotted in Figure 3 were calculated with default scripts in the YASARA library. Electrostatic potentials (ESP) *in vacuo* were calculated with YASARA to highlight the charge distribution using the recommended NOVA force field [91] and the Particle Mesh Ewald algorithm [92]. The rectangular simulation cell for the ESP calculations was 15Å from all atoms in the tetramer. No ligands were included in the calculation. Molecular images including the superpositions were calculated in YASARA [89]. Plots were generated with Excel using data imported from YASARA. The three electron density plots in Figure 3 were assembled with PyMOL (The PyMOL Molecular Graphics System, Version 1.8 (2015) Schrödinger, LLC) using electron density calculated by COOT. The final assembly of all figures was done in Photoshop.

2.2.25 Cytochrome *c* oxidase (C*c*O) activity measurements

Briefly, an aliquot of regulatory competent bovine liver C*c*O, which has the same isozyme complement as kidney C*c*O, was diluted to 3 µM final concentration in the

presence of a 40-fold molar excess of cardiolipin and 0.2 mM ATP in C*c*O measuring buffer (10 mM K-HEPES (pH 7.4), 40 mM KCl, 1% Tween 20) and dialyzed overnight at 4ºC to remove cholate bound to C*c*O during enzyme purification. Respiration of C*c*O (150 nM) was analyzed in a closed chamber equipped with a micro Clark-type oxygen electrode (Oxygraph system; Hansatech, Pentney, UK) at 25ºC in 220 µL of C*c*O measuring buffer and 20 mM ascorbate as electron donor. Increasing amounts of purified Cyt*c* variants (0-25 µM) were added, and oxygen consumption was recorded and analyzed with the Oxygraph software (Hansatech). C*c*O activity was expressed as turnover number (TN; sec^{-1}).

2.2.26 Caspase 3 activation by Cyt*c* variants

Cells from eight 150 mm plates were collected by centrifugation at 4ºC. The pellet was washed once in 5 mL of ice cold cytosol extraction buffer (20 mM HEPES, pH 7.5, 10 mM KCl, 1.5 mM $MgCl_2$, 1 mM EDTA, 1 mM EGTA, 1 mM dithiothreitol, 1 mM PMSF), resuspended gently in the same buffer, and immediately transferred to an ice cold dounce homogenizer. After 15 min of swelling on ice cells were then broken open with a B-type glass pestle, and cell breakage confirmed using a microscope. The lysates were transferred to microcentrifuge tubes and centrifuged at 4ºC and 15,000 x g for 15 min to remove nuclei and other debris. The protein concentration of the cytosolic fraction-containing supernatant was measured using the DC Assay kit (Bio Rad, Hercules, CA) and cytosolic extracts were diluted to 2 mg/mL. EnzChek Caspase-3 assay kit (Invitrogen, Carlsbad, CA) with rhodamine 110-linked DEVD tetrapeptide, an artificial substrate for caspase 3 that fluoresces upon cleavage, was used. Cytosolic extracts from Cyt*c* double knockout lung fibroblast cells (2 mg/mL concentration) were incubated with the Cyt*c*

variants (15 µg/mL) for 2.5 h at 37ºC. Caspase 3 activity was assessed in the presence or absence of the caspase 3 inhibitor by detection of fluorescence from the cleavage of the artificial caspase 3 substrate over 3 h in 30 min intervals using a Fluoroskan Ascent FL plate reader (Labsystems, Thermo Scientific, Waltham, MA), 485 nm excitation filter (14 nm band width) and 527 nm emission filter (10 nm band width). Amount of cleaved substrate was calculated from the rhodamine 110 calibration curve, and data were expressed in pmol of DEVD3 min^{-1} (mg protein)$^{-1}$.

2.2.27 Measurement of Cyt*c* redox potential

The midpoint redox potential ($E^{0'}$) was analyzed spectrophotometrically as described [75] using 2, 6 dichloroindophenol (DCIP, $E^{0'}$=237 mV) as a reference compound, which has an absorption band at 600 nm in its oxidized state. One mL of Cyt*c* solution (2 mg/mL) was mixed in a spectrophotometric cuvette with 2 mL of 50mM citrate buffer, pH 6.5, 0.1 mL of 1 mM DCIP, and 50µL of 1 mM $K_3Fe(CN)_6$ to fully oxidize Cyt*c*. Absorbances corresponding to fully oxidized Cyt*c* (A_{550}-A_{570}) and DCIP (A_{600}) were recorded using a Jasco V-570 double beam spectrophotometer. The mixture was then sequentially reduced by 1 µL additions of 5 mM ascorbate (pH 6.5), and absorbance values were acquired at each step. When readings became constant, a few grains of sodium dithionite ($Na_2S_2O_4$) were added to fully reduce Cyt*c* and DCIP. For each step, ratios of oxidized and reduced forms of both compounds were calculated. Data obtained were plotted as log($DCIP_{OX}$/$DCIP_{RED}$) versus log(Cyt_{OX}/Cyt_{RED}), yielding a linear graph with a slope of n-DCIP/n-Cyt*c* and a y-axis intercept of n-Cyt*c* / 59.2(E Cyt*c* – E DCIP). These values were used to calculate the $E^{0'}$ (mV) of Cyt*c* from the Nernst equation.

2.2.28 Measurement of rates of oxidation and reduction

The kinetics of oxidation of 15 µM ferro-Cyt*c* with 100 µM H_2O_2 and reduction of 15 µM ferri-Cyt*c* with 200 µM ascorbate was measured spectrophotometrically at 550 nm as described [55]. Briefly, WT Cyt*c* and T28E and T28A Cyt*c* mutants were reduced with sodium dithionite, and the proteins separated from the reductant through NAP5 columns. Fifteen µM Cyt*c* in 0.2 M Tris-Cl, pH 7.0 were incubated with 100 µM oxidizing agent H_2O_2 and after 10 sec, the decrease of the absorption peak at 550 nm was measured, and the amount of oxidized Cyt*c* was calculated as described above. To measure the kinetics of reduction of Cyt*c* with ascorbate, Cyt*c* variants were fully oxidized with $K_3Fe(CN)_6$ and purified using NAP5 columns. Fifteen µM ferri-Cyt*c* was added to 50 mM sodium phosphate, 25 mM sodium dithionite (Na_2SO_4), pH 7.0 and 200 µM ascorbate to a cuvette, which was then sealed from air, and the initial rate of reduction was measured at 550 nm.

2.2.29 Heme degradation assay

The degradation of heme was analyzed through dissipation of the Soret band at 408 nm using 5 µM ferri-Cyt*c* from in 50 mM phosphate buffer, pH 6.1 with 3 mM H_2O_2 as described [55]. Spectra were scanned initially after 60 seconds followed by measurements every 200 seconds.

2.2.30 Measurement of mitochondrial oxygen consumption rate tissue homogenates

Respiration of intact mitochondria in tissue homogenates was determined as described [83], using freshly harvested kidney tissues following treatment with AMPK activator and inhibitor as above, following homogenization in homogenization buffer with ten strokes. The protein concentration was determined using the DC protein assay kit

(Bio-Rad)., and diluted to 0.2 mg/mL with KCl buffer (80 mM KCl, 10 mM Tris–HCl, 3 mM MgCl, 1 mM EDTA, 5 mM potassium phosphate, 2.5 mM malate, 0.5 mg/ml BSA, pH 7.4). Mitochondrial respiration was measured at 30ºC using a Clark-type oxygen electrode as described above.

2.2.31 Tissue Treatments with AMPK activator A-769662 and inhibitor Compound C

Wild-type male mice, 2-4 months old littermates, were housed at 23°C under 12hr:12hr light:dark periods. Animals were euthanized following NIH guidelines and immediately after the animals died their kidneys taken out and placed in ice cold ST buffer containing 250 mM sucrose, 20 mM Tris, pH 7.4, 10 mM KF, 1 mM PMSF, 1 mM sodium orthovanadate, supplemented with protease inhibitor cocktail (Sigma) and phosphatase inhibitor cocktails 2 (P5726, Sigma) and 3 (P0044, Sigma) according to manufacturer's protocol. Kidneys were then minced with scissors on an ice cold glass plate and equal weight (80 mg) placed in tubes containing 2 ml buffer following treatment with either 500 µM A769662 (AMPK activator, Tocris, #3336), 3 µM Compound C (AMPK inhibitor, Sigma, P5499), or DMSO (no treatment control) for 1 h at 37ºC under shaking. Tubes were put on ice, tissues pelleted by centrifugation, and buffer replaced with 1 mL homogenization buffer (50 mM Tris-Cl, pH 7.5, 1 mM EGTA, 1% Triton-X 100, 1 mM sodium orthovanadate, 50 mM KF, 5 mM sodium pyrophosphate, 0.27 M sucrose, 0.1% β-mercaptoethanol, supplemented with protease inhibitors and phosphatase inhibitor cocktails as above, and homogenized using a Teflon dounce homogenizer by applying 60 strokes. Homogenates were centrifuged at 22,000 x g at 4ºC for 30 min and supernatants' total protein levels were quantitated using the DC protein assay kit (Bio-Rad).. Twenty µg tissue homogenates were loaded for immunoblot analyses to check for

total and phospho AMPK levels and phospho-acetyl CoA carboxylase (p-ACC) levels (AMPKα1/2 antibody (H-300), sc-25792; p-AMPKα1/2 antibody (Thr 172), sc-33524, Santa Cruz Biotechnology, Dallas, Texas, USA; p-Acetyl-CoA Carboxylase (Ser79) antibody #3661, Cell Signaling Technology, Danvers, MA, USA; antibody dilution 1:1000). Subsequently, 1 mg homogenate was used for overnight immunoprecipitation of Cyt*c*. A 10% Tris-tricine-SDS PAGE was run to analyze total and phospho AMPK levels, phospho-ACC levels, and threonine phosphorylation of immunoprecipitated Cyt*c* (using a 1:250 dilution of a set of three individual monoclonal anti-phosphothreonine antibodies, 1E11, 4D11, and 14B3, EMD Biosciences, Gibbstown, NJ). In addition, AMPK was immunoprecipitated from kidney homogenates after treatment with 500 µM A769662 for 1 h to analyze Cyt*c* co-immunoprecipitation.

2.2.32 Sucrose-density gradient isolation of mitochondria and subfractionation

Lung fibroblasts were harvested and resuspended in 10 mM NaCl, 1.5 mM $MgCl_2$, 10 mM Tris-Cl, pH 7.5. They were allowed to swell for 5 min on ice, and homogenized using a Teflon-glass homogenizer. The sucrose concentration was adjusted to 250 mM by adding 2 M sucrose and TE buffer (10 mM Tris-Cl, 20 mM EDTA, pH 7.6). The homogenate was centrifuged twice at 1,300 x g for 3 min, the supernatant collected and centrifuged at 15,000 x g for 10 min, and washed three times with 250 mM sucrose/TE buffer. The mitochondrial fraction was layered on a discontinuous sucrose gradient containing 1M sucrose and 1.7 M sucrose in TE buffer. Centrifugation was performed at 70,000 x g for 40 min at 4ºC and mitochondria retrieved from the interface. Mitochondria were washed in 250 mM sucrose/TE buffer and collected by centrifugation at 22,000 x g for 15 min to obtain highly pure mitochondria. The mitochondrial pellet was

resuspended in 20 mM sodium phosphate buffer, pH 7.2, 0.02% BSA, and allowed to swell for 20 min on ice, then 1 mM ATP and 1 mM $MgCl_2$ were added, followed by incubation on ice for 5 min, and centrifugation at 15,000 x g for 10 min at 4ºC. The supernatant contained the intermembrane space fraction and the pellet contained mitoplasts, the outer membrane fraction, and residual intermembrane space fraction.

2.2.33 Isolation and subfractionation of mitochondria from mouse kidneys

Mouse kidneys were freshly harvested and washed in ice-cold isolation buffer (10 mM Tris, 1 mM of EGTA/Tris, 200 mM sucrose, pH 7.4 adjusted with MOPS) [84]. Kidneys were minced with scissors on an ice-cold glass plate and homogenized with 20 strokes using a dounce homogenizer on ice. The homogenate was centrifuged at 600 x g for 10 min and the supernatant centrifuged at 7,000 x g for 10 min to pellet mitochondria. The mitochondrial pellet was subfractionated into an intermembrane space fraction and a mitoplast and outer membrane fraction as described above.

2.2.34 ATP assay

Lung fibroblast cells expressing Cyt*c* variants were scraped and collected and immediately stored at -80ºC until measurement. Release of ATP was performed by boiling method after addition of 300 µL of boiling buffer (100 mM Tris-Cl, pH 7.75, 4 mM EDTA), and immediate transfer of the samples to a boiling water bath for 2 min. Samples were put on ice, sonicated, diluted 300-fold, and 40 µL of the diluted samples were used to determine the ATP concentration with the ATP biolumescence assay kit HS II (Roche, Indianapolis, IN) according to the manufacturer's protocol. Data were standardized to the protein concentration using the DC protein assay kit (Bio-Rad).

2.2.35 Measurement of the mitochondrial membrane potential ($\Delta\Psi_m$)

Lung fibroblast cells expressing Cyt*c* variants were grown to 80% confluence. To assess relative changes in mitochondrial membrane potential ($\Delta\Psi_m$), cells were incubated for 30 min in phenol red-free medium containing 1 µM JC-1 (Molecular Probes). JC-1 is able to selectively enter mitochondria, is a monomer at low concentration or at low membrane potential, and emits green fluorescence. At higher membrane potential JC-1 forms aggregates that emit red fluorescence. Cells were washed with PBS and fluorescence measured with an Ascent Fluoroskan plate reader by using an excitation wavelength of 485 nm and an emission wavelength of 590 nm for red aggregates and 527 for green monomers.

2.2.36 Cell viability

Cells (100,000 per well in six-well plates) expressing Cyt*c* variants were and grown for 48 h, trypsinized, and live cells were counted after staining with trypan blue. For cell viability analyses after treatment with H_2O_2, cell number was doubled and cells were treated with 50 µM and 300 µM H_2O_2 for 24 h followed by trypan blue staining.

2.2.37 Statistical analyses

Statistical analyses were performed using MSTAT version 5.4 (N. Drinkwater, University of Wisconsin) in conjunction with the Wilcoxon rank-sum test. Data (n=3-4) are reported as means ±SD and were considered statistically significant (*) with $p<0.05$.

2.3 Results

2.3.1 Mammalian kidney cytochrome *c* is phosphorylated on Thr28 leading to 'controlled' respiration.

To test if Cyt*c* phosphorylation occurs in mammalian tissues other than heart and liver, where it is tyrosine phosphorylated, we chose kidney, an organ with a high mitochondrial capacity and the second highest oxygen consumption rate only after heart [93]. Surprisingly, Western analysis of Cyt*c* from bovine kidney detected phosphorylation on threonine (Figure 1A) but not on tyrosine (not shown). Mass spectrometry unambiguously revealed that Thr28 was phosphorylated in three independent Cyt*c* isolations analyzed (Figure 1B). This amino acid is conserved in mammals, both in the somatic and testes-specific isoform (Supplemental Figure 1A). To test the effect of Thr28 phosphorylation we measured the kinetics of Cyt*c* with isolated C*c*O. Oxygen consumption rate was 50% lower at maximal turnover for Thr28 phosphorylated versus unphosphorylated Cyt*c* (Figure 1C). Phosphorylation of Thr28 also dropped the apparent K_M of Cyt*c* in the reaction with C*c*O from 6.3 to 4.5. Similar to Tyr48 and Tyr97 phosphorylation, Thr28 phosphorylation leads to partial inhibition of respiration, or 'controlled respiration,' which we propose prevents $\Delta\Psi_m$ hyperpolarization and thus ROS production under non-stressed conditions. In order for a posttranslational modification (PTM) to be biologically relevant a significant fraction of the protein should carry the modification. Using high resolution gel electrophoresis which separates phosphorylated and unphosphorylated Cyt*c* we found that over 80% of the Cyt*c* pool was phosphorylated (Figure 1D).

2.3.2 Overexpression and purification of functional and correctly folded cytochrome *c* variants in *E. coli* cells

We and others have previously shown for tyrosine phosphorylated Cyt*c* that phosphomimetic replacement of the phosphorylatable residue with the negatively charged glutamate produces functional effects similar to those seen with the in vivo phosphorylated protein [75,94]. This approach has the advantage that large amounts of the phosphomimetic Cyt*c* can be overexpressed in bacteria and purified, and that the negative charge introduced through the glutamate residue is stable whereas attached phosphates may be lost during assays that require prolonged incubation periods or contain cytosolic extracts that contain phosphatases. We thus generated the following Cyt*c* variants based on the mouse sequence and overexpressed them in *E. coli* BL21 (DE3) cells: WT, phosphomimetic Thr28Glu, and Thr28Ala Cyt*c* as additional control, which cannot be phosphorylated. Cyt*c* variants were purified using a French press followed by anion and cation ion-exchange chromatography. Purity of Cyt*c* was confirmed by Coomassie staining (Figure 2A) and spectrophotometric analysis, with 410 nm/280 nm ratios >4 [75]. All three proteins were fully reducible and correctly folded as shown by absorption spectra measurements (Supplemental Figure 1B) and circular dichroism (Supplemental Figure 1C). Similar to our previous study [75], none of the bacterially overexpressed proteins were Ser-, Thr-, or Tyr-phosphorylated (not shown). The redox midpoint potential of Cyt*c* is approximately midway between the redox potentials of complexes III and IV, and values reported in the literature range from 220 and 270 mV [95]. We analyzed the redox midpoint potential spectrophotometrically by the equilibration method using 2,6-dichloroindophenol as the reference compound. The redox potentials for WT, Thr28Ala, and Thr28Glu were 246 mV, 221 mV, and 217 mV (Figure 2B),

suggesting that a modification on position 28 can lower the redox potential of Cyt*c*, similar as we have reported for phosphomimetic Tyr48Glu Cyt*c* [75].

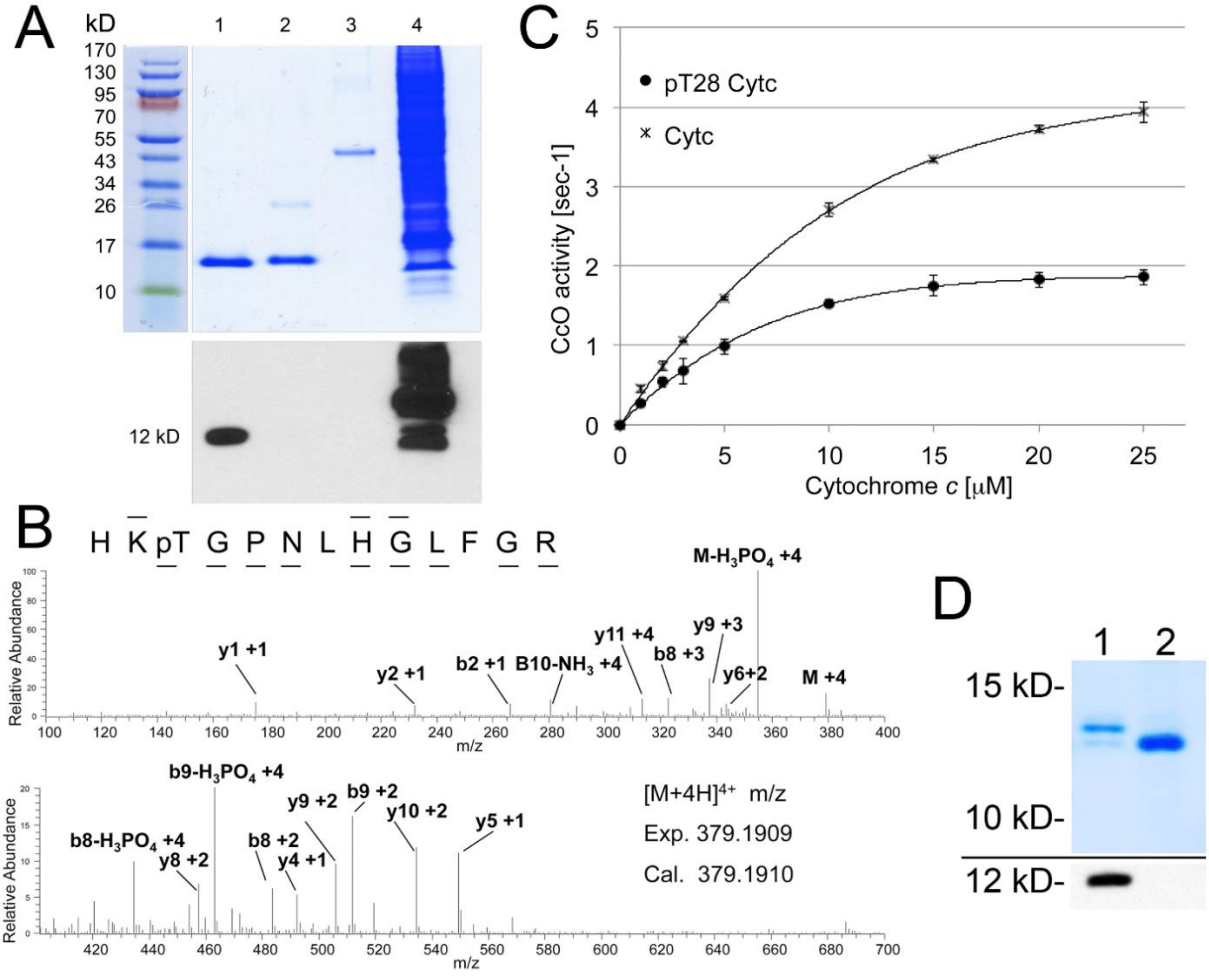

Figure 1. Kidney cytochrome *c* is phosphorylated on threonine 28 leading to controlled respiration.

(A) Purification of cow kidney Cyt*c* indicates threonine phosphorylation. Lane 1, kidney Cyt*c*; lane 2, cow heart Cyt*c* (Sigma); lane 3, ovalbumin (Western negative control); lane 4, EGF treated cell extract (Western positive control). Top, Coommassie gel; bottom anti-phospho-Thr Western blot.

(B) Nano-LC/ESI/MS/MS spectrum of HKpTGPNLHGLFGR reveals phosphorylation of Thr28. The phosphorylation site was unambiguously assigned by fragment ions y10 and y11. The sequence of the peptide was assigned by b2, b8, b9, y1, y2, y4, y5, y6, y8, y9, and y10.

(C) In vitro cytochrome *c* oxidase activity with in vivo phosphorylated pThr28 (pT28) is 50% reduced at maximal turnover compared to unphosphorylated Cyt*c*.

(D) High resolution gel electrophoresis indicates that 83% of the Cyt*c* pool is phosphorylated (lane one, upper band). Lane 2, unspecific phosphatase treatment of Cyt*c* collapses the upper band.

2.3.3 Phosphomimetic cytochrome *c* displays a significantly decreased reaction rate with isolated cytochrome *c* oxidase (C*c*O)

We showed that in vivo phosphorylated Cyt*c* displayed an approximately 50% inhibition in the reaction with isolated bovine liver C*c*O (Figure 1C). To demonstrate that Thr28Glu is a good model for Thr28 phosphorylated Cyt*c* we first analyzed its activity in the reaction with purified C*c*O. As shown in Figure 2C, we found that respiration rates of phosphomimetic Thr28Glu and Thr28Ala Cyt*c* were 73% and 51% reduced, respectively, indicating that Thr28Glu Cyt*c* serves as a useful model. The apparent K_M of Cyt*c* in the reaction with C*c*O was 7.8, 9.3, and 4.7 for unphosphorylated WT, Thr28Glu, and Thr28Ala Cyt*c*, respectively. The fact that the inhibitory effect of the phosphomimetic substitution is even more pronounced than that observed with in vivo phosphorylated Cyt*c* may be due to the subfraction (about 20%) of unphosphorylated Cyt*c* present when isolated from kidneys.

2.3.4 Thr28Glu cytochrome *c* is capable to trigger caspase-3 activation but shows distinct features in its ROS-related functions

To test the possible effect of Thr28 phosphorylation on apoptotic function, we analyzed the ability of the Cyt*c* variants to trigger apoptosis by measuring downstream activation of caspase-3 using a cell-free caspase assay. Cyt*c* mutants were incubated with cytosolic fractions prepared from mouse lung fibroblasts in which both the somatic and testes-specific isoforms of Cyt*c* were knocked out [77]. The Thr28Glu mutant was able to activate caspase-3 similar to wild-type Cyt*c* protein (Figure 2D) and Thr28-phosphorylated Cyt*c* (Supplemental Figure 2), indicating that Thr28 phosphorylation of

Cyt*c* does not affect the function of Cyt*c* at the level of apoptosome formation. Other functions of Cyt*c* include ROS scavenging, such as reduction by superoxide to regenerate oxygen or oxidation by H_2O_2. We therefore tested the ability of Cyt*c* in the reaction with H_2O_2 and with the reductant ascorbate. To analyze the former, ferro-(Fe^{2+})-Cyt*c* variants were oxidized in the presence of 100 µM H_2O_2. The Thr28Glu phosphomimetic mutant was oxidized at a rate similar to WT Cyt*c*, while Thr28Ala mutant was oxidized at a 2.7-fold higher rate (Figure 2E). At higher ROS load Cyt*c* can lose its functionality through oxidative modifications, which can be monitored through a decrease in the absorption of the heme Soret band at 408 nm present in intact Cyt*c*. After addition of excess H_2O_2 (3 mM) Thr28Glu Cyt*c* was more resistant to degradation by excess H_2O_2 than the wild-type, while the Thr28Ala mutant was degraded more rapidly (Figure 2F), suggesting that the introduction of a negative charge in position 28 stabilizes the protein. To determine the rate of Cyt*c* reduction, ferri-(Fe^{3+})-Cyt*c* variants were reduced in the presence of 200 µM ascorbate. Thr28Glu Cyt*c* was reduced at about twice the rate compared to WT and Thr28Ala Cyt*c* (Figure 2G), suggesting that it can act as a superior electron acceptor and scavenger.

Cardiolipin (CL) oxidation is a pro-apoptotic function of Cyt*c*. Native Cyt*c* possesses a low degree of peroxidase activity, which increases when CL binds to Cyt*c* causing partial unfolding [96]. To assess peroxidase activity of Cyt*c*, the rate of Amplex Red oxidation by CL-peroxide was analyzed in the presence of H_2O_2. H_2O_2 is a poor substrate for Amplex Red oxidation whereas oxidized CL species are good substrates. At higher tetralinoleyl-CL(TOCL)/Cyt*c* ratios Thr28Glu Cyt*c* showed significantly reduced peroxidase activity compared to WT (Figure 2H). Interestingly, the Thr28Ala mutant had

the highest peroxidase activity at all ratios, suggesting that it unfolds more easily compared to WT and Thr28Glu Cyt*c*.

2.3.5 High resolution X-ray crystallography and molecular dynamics reveal structural features of the Thr28 epitope.

In order to gain a better understanding of the structure-function relationship of the Thr28 epitope we crystalized all three mouse Cyt*c* variants under oxidizing conditions and obtained crystals that diffracted at a resolution of 1.12 Å, 1.36 Å, and 1.30 Å for WT, Thr28Ala, and Thr28Glu Cyt*c*. The WT structure has the highest resolution of any mammalian Cyt*c* structure. As expected, the crystal structures of WT, Thr28Ala and Thr28Glu are overall similar (Figure 3A, D, and G and Supplemental Table 1). To explore possible differences in their solution structures, molecular dynamics simulations were performed on the A-chain from the three protein structures as well as on a model of phosphorylated Cyt*c* with the phosphate group added to Thr28 in the WT chain-A using COOT (PDB code: Tpo28). In all four simulations, the C□-chain from the final solution structure after 200 ns superposed well with the beginning crystal structure except for the Thr28-containing loop 22-30 (Fig. 3: A, B, D, E, G, H, J, and K), which also had the highest root mean square fluctuations (RMSF) except for the N- and C-termini (Figure 3C, F, I, and L). In all 4 simulations, the surface loop adopted an alternate conformation, which moved the Cα atom of residue 28 about 5 Å from its starting position. Surprisingly, in the Thr28Ala simulation, the loop paused at the same conformation as the others but then continued to move until it reached a conformation after 200 ns that put Ala28 11.9 Å from its starting position (Figure 3E). These differences may explain the structural instability of this mutant. In contrast Thr28Glu Cyt*c* recapitulates the functional effects seen with in vivo phosphorylated Cyt*c*. As expected, electrostatic potential (ESP) calculations show

that the Thr28Glu mutant has a negative ESP region that is larger than WT and only exceeded by the Thr28Tpo model (Supplemental Figure 4B, C, and D).

2.3.6 Introduction of Thr28Glu cytochrome *c* into cytochrome *c* double knockout cells reduces oxygen consumption rate, the mitochondrial membrane potential, and ROS.

To test the effect of phosphomimetic substitution of Cyt*c* on mitochondrial parameters in intact cells we generated stably transfected cell lines, transfected with empty vector (EV) control and WT, Thr28Glu, and Thr28Ala Cyt*c*, using mouse lung fibroblast in which both the somatic and testes-specific Cyt*c* isoforms have been knocked out. Double knockout is required since cultured cells lacking somatic Cyt*c* induce the expression of the testes isoform, restoring mitochondrial respiration [77]. Expression levels of WT and Thr28Glu Cyt*c* were comparable between different clones whereas protein levels of Thr28Ala Cyt*c* was less compared to the other Cyt*c* variants (the clone with the highest expression levels was used for subsequent experiments, Figure 2I), suggesting that higher expression levels of this mutant may interfere with cellular functions or that protein turnover is higher. As previously reported, Cyt*c* knockout interferes with complex I and IV assembly [97], which is reduced upon reintroduction of the three Cyt*c* variants (Figure 2I). Determination of cell growth showed that WT and Thr28Glu Cyt*c* expressing cells grew equally well whereas Thr28Ala Cyt*c* expressing cells showed a 27% reduced growth rate versus WT (Fig. 2J) (see Discussion). We first analyzed intact cell respiration. Strikingly, cells expressing Thr28Glu phosphomimetic Cyt*c* showed 60% reduced respiration rates (Figure 2K) matching those results obtained with purified C*c*O in vitro (Figures 1C and 2C). This finding is of importance because it suggests that a modification of the small electron carrier Cyt*c* can control overall flux in the ETC, a scenario that has not been reported or considered in the past. Consequently, a reduction of the respiration

rate should translate into a reduced mitochondrial membrane potential $\Delta\Psi_m$. Analysis with the voltage-dependent probe JC-1 showed that Thr28Ala and Thr28Glu expressing cells showed 15% and 31% reduced fluorescence compared to WT (Figure 2L), indicating a reduction of $\Delta\Psi_m$. Given the direct connection of $\Delta\Psi_m$ with ROS production at complexes I and III [98], we predicted that Thr28Glu expressing cells should exhibit reduced ROS levels. Using the mitochondrial ROS probe MitoSox we found that fluorescent signals were reduced by 35-40% in cells expressing Thr28Glu and Thr28Ala Cyt*c* compared to WT, indicating reduced ROS levels (Figure 2M). ATP levels were reduced by 6% and 28% for cells expressing Thr28Ala and Thr28Glu, respectively (Figure 2N). To test if cells expressing Thr28Glu Cyt*c* are better protected from H_2O_2 exposure, cell viability was determined after treatment with H_2O_2. Thr28Glu Cyt*c* expressing cells showed higher viability when treated with low concentration of H_2O_2, but viability matched with WT Cyt*c* expressing cells at higher H_2O_2 concentration (Figure 2O). This observation suggests that Thr28Glu Cyt*c* protects the cells from mild oxidative stress. These data suggest that modification of Cyt*c* Thr28 regulates ETC flux, which in turn affects $\Delta\Psi_m$ and ROS.

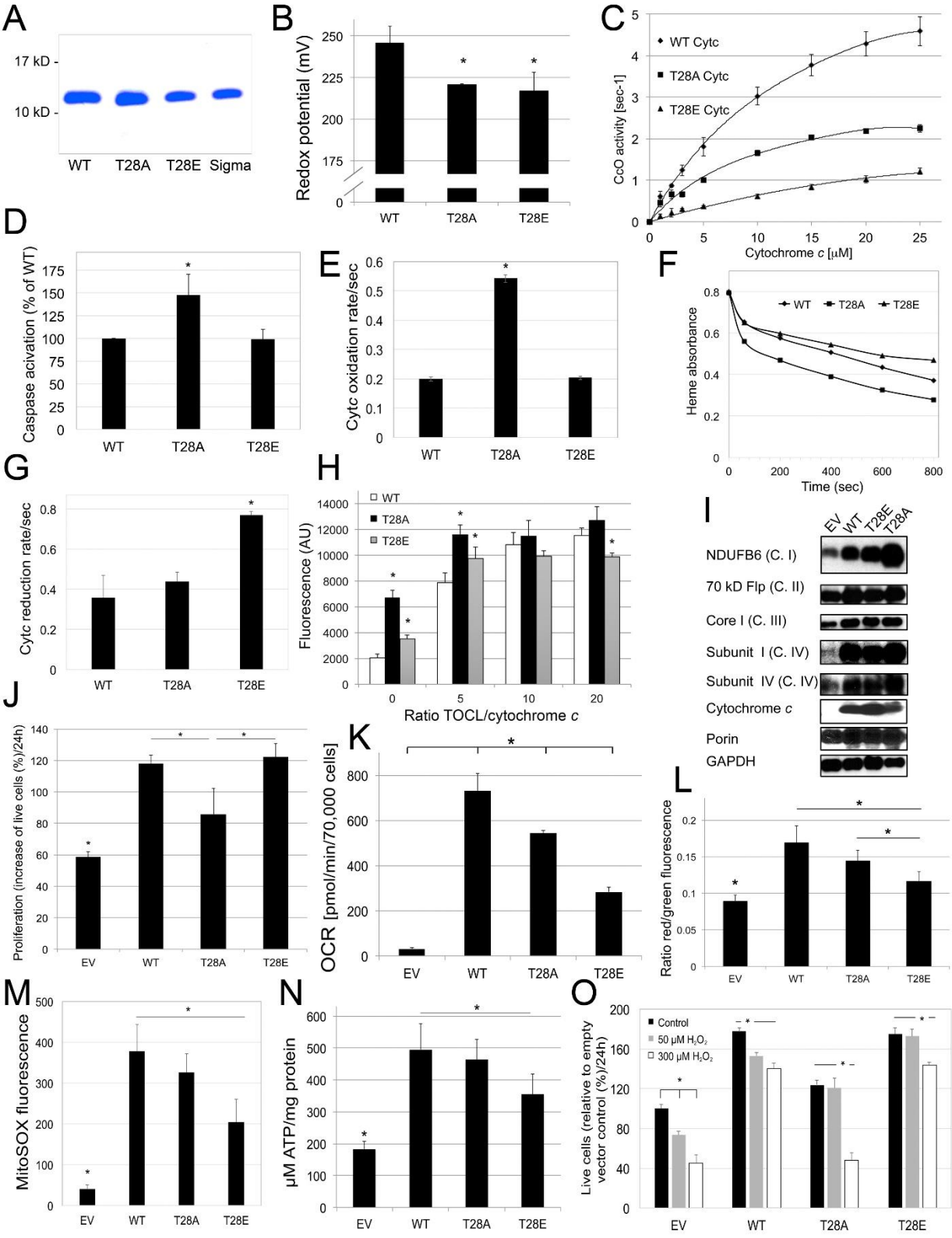

Figure 2. Phosphomimetic Thr28Glu cytochrome *c* shows unique features in vitro and after reintroduction into cytochrome *c* double knockout cells.

(A) Coomassie gel of bacterially overexpressed and isolated wild-type (WT), Thr28-phosphorylated Cyt*c* (pT28), Thr28Glu (T28E), and Thr28Ala (T28A) Cyt*c* indicates that the proteins were purified to homogeneity.

(B) Redox potential is reduced in the Thr28Glu and Thr28Ala mutants compared to WT.

(C) O_2 consumption rates of Cyt*c* in the reaction with cow cytochrome *c* oxidase were 73% and 51% reduced for Thr28Glu and Thr28Ala Cyt*c*.

(D) In vitro caspase 3 activity is unaltered in Thr28Glu Cytc whereas it is increased with the Thr28Ala mutant.

(E) Oxidation rate of WT and Thr28Glu Cyt*c* in the presence of H_2O_2 is similar whereas the Thr28Ala mutant shows increased rates.

(F) Compared to WT, loss of the heme group by excess H_2O_2 is decreased and increased for Thr28Glu and Thr28Ala Cyt*c*, respectively. Shown are representative heme destruction curves.

(G) Thr28Glu Cyt*c* reduction rate in the presence of ascorbate is increased compared to WT and Thr28Ala Cyt*c*.

(H) Thr28Glu Cyt*c*-mediated cardiolipin oxidation is decreased at highest TOCL/Cyt*c* ratios compared to WT and Thr28Ala Cyt*c.*

(I) Western blot of Cyt*c* double knockout lung fibroblasts stably transfected with empty vector (EV) and WT, Thr28Ala, and Thr28Glu expression constructs.

(J) Proliferation rates of stably transfected lines were determined by cell counts.

(K) Intact cell oxygen consumption rates (OCR) are decreased in both Cyt*c* mutants.

(L) Mitochondrial membrane potential as determined by JC-1 fluorescence was decreased in cells expressing Thr28Glu versus WT and Thr28Ala Cyt*c*.

(M) Basal mitochondrial reactive oxygen species generation as determined with MitoSOX is decreased in cells expressing Thr28Glu Cyt*c* compared to WT.

(N) ATP levels determined with the bioluminescent method were decreased in cells expressing Thr28Glu Cyt*c* compared to WT.

(O) Live cell counts after treatment with H_2O_2 indicate that Thr28Glu expressing cells are better protected at intermediate H_2O_2 levels compared to WT whereas Thr28Ala expressing cells show decreased survival at all concentrations.

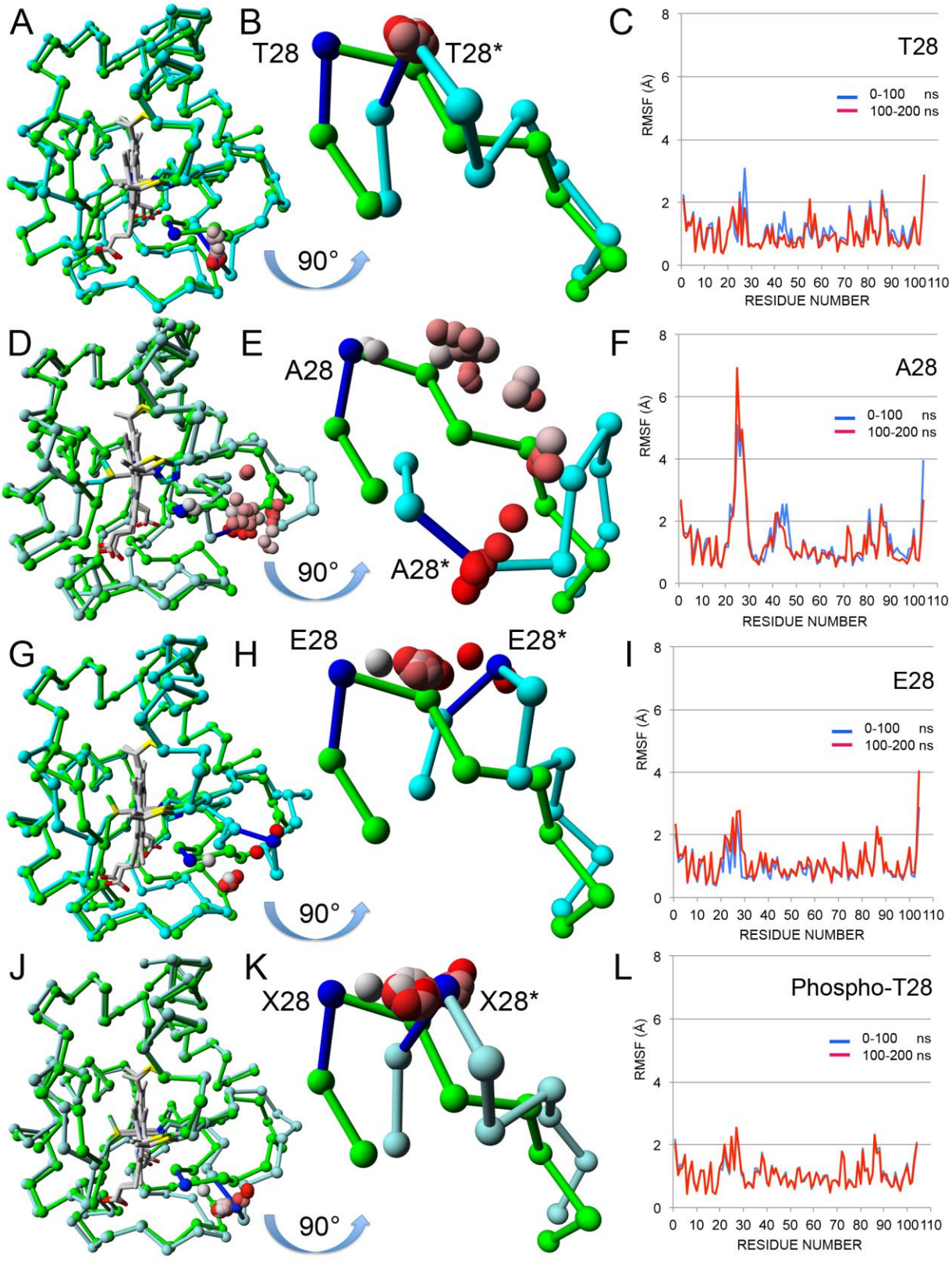

Figure 3. Structural and molecular dynamics analyses.

(A) Chain-A from the WT crystal structure (5C0Z.pdb) before (green) and after (cyan) 200 ns of molecular dynamics are shown as C□ tracings superimposed using only main chain atoms. The hemes (Hec201) are shown in gray. The average T28 C□ positions for the 39 intermediate 5 ns steps between the two endpoints are shown as spheres colored in a gradient from gray (5 ns) to red (195 ns).

(B) The mobile loop (amino acids 22-30) from Figure 3A is shown in higher detail after rotation by 90° about its horizontal axis to generate a "bottom-up" view. The C□ atom for the starting (T28) and ending (T28*) structures are colored blue. The intermediate C□ atoms (gray to red) all cluster about T28* showing that the loop jumps immediately to its minimum energy position and stays there. The distance between T28 C□ and T28* C□ is 4.5 Å.

(C) The root mean square fluctuations (RMSF) for the first 100 ns (blue line) and the second 100 ns (red line) by residue are plotted together. Two RMSF values in the first 100 ns (Lys27, Ala44) are noticeably lower in the second 100 ns.

(D) Chain-A from the T28A crystal structure (5C9M.pdb) before (green) and after (cyan) 200 ns of molecular dynamics. See Figure 3A for details.

(E) Equivalent to Figure 3B except the two loops are from Figure 3D. Over the 200 ns, the C□ atom of Ala28 pauses at 4 distinct intermediate positions before clustering around the final position. The distance between A28 C□ and A28* C□ is 11.9 Å.

(F) Equivalent to Figure 3C for T28A Cyt*c*. The RMSF values for Ala44 are lower in the second 100 ns but those for Lys27 are significantly higher in the second 100 ns, in fact the highest seen in all four RMSF plots.

(G) Chain-A from the T28E crystal structure (5DF5.pdb) before (green) and after (cyan) 200 ns of molecular dynamics. See Figure 3A for details.

(H) Equivalent to Figure 3B except the two loops are from Figure 3G. Over the 200 ns, the C□ atom of Glu28 clusters at a midway position before moving to its final position near the end of the simulation. The distance between E28 C□ and E28* C□ is 7.2 Å.

(I) Equivalent to Figure 3C for T28E Cyt*c*. The RMSF values for Ala44 are of average size and similar for both halves of the simulation. The RMSF values for the loop containing Glu28 are higher than average but similar for both halves of the simulation.

(J) The C□ tracings of chain-A from the WT crystal structure (5C0Z.pdb) with a phosphate group modeled onto Thr28 are shown superposed before (green) and after (cyan) 200 ns of molecular dynamics. See Figure 3A for details.

(K) Equivalent to Figure 3B except the two loops are from Figure 3J. Over the 200 ns period, the C□ atom of Tpo28 moves quickly to the final position and clusters around it. The distance between X28 C□ and XT28* C□ is 5.2 Å.

(L) Equivalent to Figure 3C for the T28PO model. The RMSF values for the loop containing Glu28 are higher than average but similar for both halves of the simulation.

2.3.7 AMPK interacts with and phosphorylates cytochrome *c* on Thr28

To identify a kinase candidate that targets Cyt*c* for Thr28 phosphorylation we first used the online tool Scansite [99] for in silico prediction of possible Cyt*c* binding motifs of signaling molecules. Interestingly, Thr28 was predicted to be an AMPK phosphorylation site. To test this possibility we first performed an in vitro kinase assay with commercially available AMPK and unphosphorylated WT Cyt*c* as substrate to see if this reaction can, in principle, take place. As shown in Figure 4A, Cyt*c* was phosphorylated in a specific and AMPK-dependent manner, which could be further accelerated by addition of AMPK activator AMP (Figure 4B). We next confirmed by mass spectrometry that Thr28 was the site of in vitro AMPK phosphorylation (Figure 4C). In order for AMPK to phosphorylate Cyt*c* in kidney the proteins have to physically interact inside the cell. Under basal conditions, co-immunopreciptation experiments using extracts from total mouse kidney tissue as well as highly purified mitochondria shows interaction of AMPK with Cyt*c* (Figure 4D). Furthermore, submitochondrial fractionation of highly purified mitochondria indicates that AMPK and its activated phosphorylated form is present in the mitochondrial intermembrane space (Figure 4E, lane 2), as is Cyt*c*. Finally, activation and inhibition of AMPK in mouse kidney tissue using A769662 and Compound C, as confirmed by phosphorylation of AMPK target phospho-acetyl-CoA carboxylase (Figure 4F), results in increased and decreased threonine phosphorylation of Cyt*c*, respectively (Figure 4G), which inversely correlates with intact mitochondrial respiration rates (Figure 4H), mirroring data presented in Figures 1 and 2. It is important to note that no such effects were observed using liver tissue (data not shown), suggesting tissue-specific differences in the regulation of Cyt*c*, which agrees with our previous studies demonstrating that liver Cyt*c*

is Tyr48 phosphorylated.

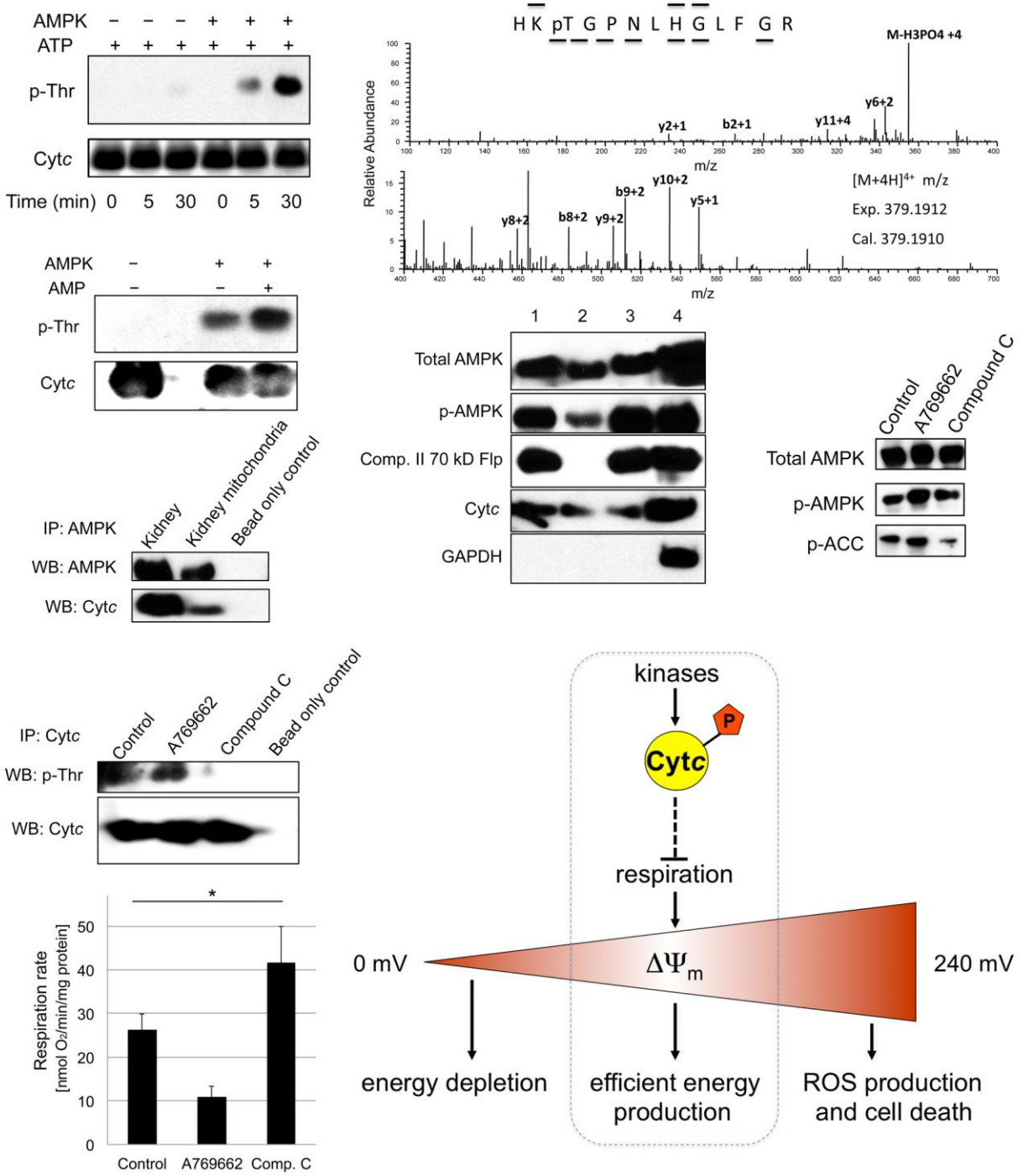

Figure 4. AMPK interacts with and phosphorylates cytochrome *c* on Thr28.

(A) In vitro AMPK kinase assay with cow heart Cyt*c*, conducted in the absence of AMPK activator AMP, shows a time-dependent increase of threonine phosphorylation as determined by Western analysis.

(B) In vitro AMPK kinase assay with cow heart Cyt*c* shows an increase of threonine phosphorylation in the presence of AMPK activator AMP.

(C) Cyt*c* subjected to in vitro AMPK kinase assay as in (A) is phosphorylated on Thr28 as determined by the Nano-LC/ESI/MS/MS spectrum of HKpTGPNLHGLFGR. The phosphorylation site was unambiguously assigned by fragment ions y10 and y11. The sequence of the peptide was assigned by b2, b8, b9, y2, y5, y6, y8, y9, and y10.

(D) Immunoprecipitation (IP) of AMPK from total mouse kidney extracts and purified mitochondrial extracts shows interaction of AMPK with Cyt*c*.

(E) Submitochondrial fractionation of sucrose gradient purified mouse kidney mitochondria shows AMPK and p-AMPK localization to the mitochondrial intermembrane space (IMS). Lane 1, mitochondrial lysate; lane 2, intermembrane space; lane 3, pellet after outer mitochondrial membrane permeabilization containing outer mitochondrial membrane, mitoplasts and residual IMS; lane 4, kidney tissue homogenate.

(F) Incubation of mouse kidney tissue with AMPK activator A769662 and inhibitor Compound C leads to activation and inhibition of AMPK, respectively, as deduced by AMPK target phospho-acetyl-CoA carboxylase (p-ACC).

(G) Pull-down of Cyt*c* from mouse kidney tissue after treatment with AMPK activator A769662 and inhibitor Compound C leads to an increase and decrease of Cyt*c* threonine phosphorylation, respectively.

(H) Incubation of mouse kidney tissue with AMPK activator A769662 and inhibitor Compound C leads to decreased and increased intact mitochondrial respiration as determined in tissue homogenates.

(I) Model of the regulation of electron transport chain activity through phosphorylation of Cyt*c*. Under healthy conditions Cyt*c* is phosphorylated, leading to a partial inhibition of mitochondrial respiration. This in turn maintains healthy intermediate membrane mitochondrial potentials ($\Delta\Psi_m$) that are sufficient for effective energy production but prevent the generation of ROS, which occurs at pathologically high $\Delta\Psi_m$ values.

2.4 Discussion and summary

Very little is known about the regulation of mitochondrial oxidative phosphorylation by cell signaling. We have previously reported two distinct tyrosine phosphorylation sites on Cyt*c* from mammalian heart and liver tissue. The current report functionally characterizes a third tissue-specific phosphorylation site, Thr28 mapped on Cyt*c* purified from kidney. The same site was also mapped, but not further studied, in a high-throughput mass spectrometry study using resting human skeletal muscle [100], suggesting that Thr28 can be targeted to regulate ETC function beyond kidney tissue. Here, we have isolated Cyt*c* from kidney in which the majority (between ~60-80%, depending on the preparation) of the protein is phosphorylated at Thr28. In addition, we have mutated Thr28 to glutamic acid, a phosphomimetic amino acid, and alanine, a non-phosphorylatable control mutation, to further characterize the effects of this phosphorylation in vitro and in cultured murine lung fibroblast cells lacking both Cyt*c* isoforms, the only Cyt*c* double knockout cell line available.

Bovine in vivo phosphorylated and unphosphorylated Cyt*c* as well as overexpressed mouse WT, Thr28Glu, and Thr28Ala Cyt*c* generated hyperbolic kinetics in the reaction with purified bovine liver C*c*O. All Cyt*c* species exhibited K_M values from 4 to 10 micromolar. Maximal turnover was reduced by 50% and 73% for in vivo phosphorylated and phosphomimetic Cyt*c*, respectively. Furthermore, expression of phosphomimetic Thr28Glu Cyt*c* led to a reduction of respiration in intact cells suggesting for the first time that modification of the small electron carrier can control overall ETC flux. These findings are consistent with the concept that phosphorylation of mitochondrial proteins, in general, down-regulates whereas dephosphorylation activates mitochondrial

function [101]. Reduced respiration rates both in vitro with purified C*c*O and in intact cells expressing Thr28Glu Cyt*c* may be a result of the observed change in the redox midpoint potential as well as structural changes of the protein. Thr28 lies in the center of an unusual structural element termed "negative classical gamma turn," which is composed of residues 27-29 and important for the stability of Cyt*c* [102]. Thr28 is a surface residue close to the solvent exposed and accessible tip of the heme group that mediates electron transfer to C*c*O. It is located on the frontal right side of the molecule in the conventional view (Figure 3A), which is part of the circular, positively charged epitope surrounding the heme crevice with which Cyt*c* binds to the corresponding negatively charged epitope on C*c*O [12]. Interestingly, in this computational Cyt*c*-C*c*O docking model, Thr28 is located at the interface of catalytic subunits I and II and nuclear encoded subunit VIIc, with closest distances of <6Å with Lys47 of subunit VIIc, and of <7Å with Asp50 of subunit I and Trp104 and Ser202 of subunit II (Supplemental Figure 4G). Two of the four C*c*O residues are particularly noteworthy. Asp50 is one of only a handful of residues in the entire C*c*O complex that have noticeably different geometries between the reduced and oxidized state in the crystal structure [103]. In addition, Asp50 is located next to another flexible amino acid, Asp51, which, when mutated to Asn, blocks proton pumping of the enzyme and was proposed to be the proton ejection site of C*c*O [104]. Phosphorylation of Thr28 may interfere with the outward movement of the Asp50-Asp51 region and thus the opening of the proposed proton exit channel during reduction of C*c*O. This would lead to inhibition of C*c*O by inhibiting electron transfer-coupled proton pumping. Alternatively, repulsion between phospho-Thr28 and Asp50 may result in suboptimal binding to C*c*O, causing reduced respiration rates. The second interesting interaction site on C*c*O is Trp104, which

is the site of C*c*O where electrons from Cyt*c* enter C*c*O before reaching the first metal center, the binuclear Cu_A site. Spatial interference upon Cyt*c* Thr28 phosphorylation with Trp104, which is essential for catalysis, could also explain reduced activity. Analogous considerations may also be applicable for the interaction of Cyt*c* with bc_1 complex.

We have previously shown that phosphomimetic Tyr48Glu Cyt*c* is incapable of downstream caspase activation [75]. In contrast, phosphorylation of Cyt*c* Thr28 or its phosphomimetic substitution does not interfere with the ability of Cyt*c* to trigger downstream caspase activation. This difference agrees with the observation that the Tyr48 epitope is directly involved in the interaction of Cyt*c* with Apaf-1, whereas the Thr28 epitope is not [105].

We observed threonine phosphorylation of Cyt*c* from kidney but not from liver tissue, where Cyt*c* is phosphorylated on Tyr48 under basal conditions [74]. Signaling molecules including AMPK are expressed in a tissue-specific manner, which may in part explain tissue-specific differences in cell signaling. Trimeric AMPK consists of three subunits, each of which composed of several isoforms. The primary isoforms found in kidney are α1, β1 and β2, and γ1 and γ2 [106]. Future work should identify which AMPK subunit composition is present in kidney mitochondria. Cell signaling also operates differently in different organisms. Ser/Thr/Tyr-phosphorylations are most common in mammals whereas His/Arg/Lys/Asp-phosphorylations are common in bacteria but not in mammals. A recent study compared 285 Cyt*c* sequences across all phyla from humans to bacteria [107]. Overall, threonine is the most common amino acid at position 28 and conserved in mammals. However, in some non-mammalian organisms five other amino acids can also be found, namely Gln, Val, Ile, Ser, and even the phosphomimetic Glu,

which is present in several plants including potatoes and tomatoes. Interestingly, alanine is not among the residues evolutionarily tolerated in this position. We found that Thr28Ala Cyt*c* has a higher ability to activate downstream caspases and unfolds more easily, which increases CL oxidation. Its instability compared to WT and Thr28Glu Cyt*c* is also suggested in the respective circular dichroism spectra (Supplemental Figure 1C, see lower wavelength range). In addition, Thr28Ala Cyt*c* is most rapidly oxidized and degraded in the presence of H_2O_2. These features of the Thr28Ala mutant may explain why it was evolutionarily selected against. Structural analysis of all three Cyt*c* variants shows that the amino acids comprising the negative classical gamma turn element display by far the highest root-mean-square deviation values compared to any other Cyt*c* sequence, suggesting that the Thr28 epitope is the most flexible element of the entire molecule. A plot of the average temperature factors, which for these high resolution structures are a reasonable measure of local mobility, also showed that the highest relative values, other than at the termini, occurred at the 22-30 loop for all three structures. Furthermore, molecular dynamics simulations of crystalized Thr28Ala Cyt*c* produce a structure in which the Thr28 Cα atom is moved by 11.9 Å, over twice as far compared to WT, Thr28Glu, and modeled phospho-Thr28 Cyt*c* (Figure 3). These findings collectively suggest that alanine was evolutionarily selected against, since it introduces additional flexibility, likely due to its small size, at a site near the heme crevice leading to a detrimental reduction of protein stability and interference with its multiple functions. This may also at least in part account for the finding of lower Cyt*c* protein levels in cells expressing this mutant. Another evolutionarily forbidden substitution,Thr28Asp, which introduces a negative charge, also generates “rogue” functional changes in Cyt*c* as seen

in the reaction with C*c*O that are even opposite [108] of what we report with in vivo phosphorylated Cyt*c*, while glutamate replacement as used here, produces the same functional effects as phosphorylated Cyt*c*. These findings collectively suggest that some amino acids such as alanine and aspartate were evolutionarily selected against, since they alter the functions of Cyt*c*. Alanine replacement introduces additional flexibility, likely due to its small size, at a site near the heme crevice leading to a detrimental reduction of protein stability and interference with its multiple functions. This may also at least in part account for the finding of lower Cyt*c* protein levels in cells expressing this mutant.

Our studies suggest that AMPK targets Cyt*c* for Thr28 phosphorylation within the mitochondria. AMPK is one of the most important and evolutionarily oldest metabolic sensors and regulators [109]. It is implicated in human disease including diabetes, where its activity is impaired in several organs including the kidneys [110]. Generally, AMPK promotes catabolic processes, and it is activated by phosphorylation and allosterically under conditions when ATP levels drop and AMP levels increase. However, our understanding of the role of AMPK specifically in the kidney is in its infancy [111], and there are reports suggesting that it operates differently in this organ compared to other tissues. For example, AMPK is already active in kidney under basal conditions and shows a paradoxical decrease in activity in a rat kidney ablation and infarction model [112], a condition when energy depletion and thus demand is maximal. In cells from patients with hereditary leiomyomatosis renal cell cancer, the Krebs cycle is inhibited, which also leads to a paradoxical decrease of AMPK activity [113]. The high basal activity of AMPK also observed in this study (Figure 4F) may be due to the fact that kidneys are always active and rely heavily on oxidative phosphorylation [93]. Consistent with our findings that AMPK-

mediated Cyt*c* phosphorylation partially suppresses mitochondrial respiration, it was shown in human renal proximal tubular epithelial cells that additional activation of AMPK with metformin results in a significant reduction of cellular respiration [114]. We propose a model, shown in Figure 4I, that a central role of Cyt*c* Thr28 phosphorylation in kidney is to maintain optimal intermediate $\Delta\Psi_m$ levels, which allow efficient energy production but prevent ROS generation because ROS are produced at high $\Delta\Psi_m$ levels (reviewed in [115]. In line with our concept, it was shown in rats subjected to renal ischemia/reperfusion injury that application of a high dose of AMPK activator AICAR shortly before ischemia significantly improves cell survival [116]. Cyt*c* purified from ischemic kidney is dephosphorylated (not shown) similar to Cyt*c* isolated from ischemic brain [71]. This would allow maximal ETC flux, $\Delta\Psi_m$ hyperpolarization, and ROS production during reperfusion when ETC function is reinstated due to reintroduction of oxygen. We have shown that neuroprotective insulin treatment prior to brain ischemia/reperfusion leads to Cyt*c* Tyr97 phosphorylation, which also decreases respiration, resulting in suppression of the release of Cyt*c* from the mitochondria, and a 50% reduction of neuronal death [71]. It will be interesting to see in future studies if AICAR treatment maintains Cyt*c* Thr28 phosphorylation during ischemia in kidney, alleviating ETC hyperactivation during reperfusion.

In conclusion, all three functionally studied Cyt*c* phosphorylations to date, Tyr97, Tyr48, and Thr28, lead to a partial inhibition in the reaction with C*c*O, or 'controlled respiration' (Figure 4I). We propose that this mechanism provides a basis for the maintenance of 'healthy' intermediate $\Delta\Psi_m$ levels under normal conditions. This, in turn, prevents excessive ROS production that occurs at high $\Delta\Psi_m$ levels under conditions of

stress when mitochondrial proteins become dephosphorylated, allowing maximal ETC flux, $\Delta\Psi_m$ hyperpolarization, excessive ROS, and cell death. Although all 3 known Cyt*c* phosphorylations limit respiration, the choice of site in a particular tissue may depend on tissue-specific metabolic differences or on additional effects of the phosphorylation, such as the participation of Cyt*c* in apoptosis.

2.5 Supplemental Figures

```
                10        20        30        40        50        60        70        80        90        100
                *         *         *         *         *         *         *         *         *         *
Human     GDVEKGKKIFIMKCSQCHTVEKGGKHKTGPNLHGLFGRKTGQAPGYSYTAANKNKGIIWGEDTLMEYLENPKKYIPGTKMIFVGIKKKEERADLIAYLKKATNE
Horse     GDVEKGKKIFVQKCAQCHTVEKGGKHKTGPNLHGLFGRKTGQAPGFSYTDANKNKGITWKEETLMEYLENPKKYIPGTKMIFAGIKKKTEREDLIAYLKKATNE
Bull      GDVEKGKKIFVQKCAQCHTVEKGGKHKTGPNLHGLFGRKTGQAPGFSYTDANKNKGITWGEETLMEYLENPKKYIPGTKMIFAGIKKKGEREDLIAYLKKATNE
Pig       GDVEKGKKIFVQKCAQCHTVEKGGKHKTGPNLHGLFGRKTGQAPGFSYTDANKNKGITWGEETLMEYLENPKKYIPGTKMIFAGIKKKGEREDLIAYLKKATNE
Goat      GDVEKGKKIFVQKCAQCHTVEKGGKHKTGPNLHGLFGRKTGQAPGFSYTDANKNKGITWGEETLMEYLENPKKYIPGTKMIFAGIKKKGEREDLIAYLKKATNE
Dog       GDVEKGKKIFVQKCAQCHTVEKGGKHKTGPNLHGLFGRKTGQAPGFSYTDANKNKGITWGEETLMEYLENPKKYIPGTKMIFAGIKKTGERADLIAYLKKATKE
Mouse     GDVEKGKKIFVQKCAQCHTVEKGGKHKTGPNLHGLFGRKTGQAAGFSYTDANKNKGITWGEDTLMEYLENPKKYIPGTKMIFAGIKKKGERADLIAYLKKATNE
Rat       GDVEKGKKIFVQKCAQCHTVEKGGKHKTGPNLHGLFGRKTGQAAGFSYTDANKNKGITWGEDTLMEYLENPKKYIPGTKMIFAGIKKKGERADLIAYLKKATNE
Bat       GDVEKGKKIFVQKCAQCHTVEKGGKHKTGPNLHGLFGRKTGQAPGFSYTDANKNKGITWGEATLMEYLENSKKYIPGTKMIFAGIKKSAERADLIAYLKKATNE
Dolphin   GDIEKGKKIFVQKCAQCHTVEKGGKHKTGPNLHGLFGRKTGQAVGFSYTDANKNKGITWGEETLMEYLENPKKYIPGTKMIFAGIKKKXERADLIAYLKKATNE

Bull-T    ADAEAGKKIFIQKCAQCHTVEKGGKHKTGPNLWGLFGRKTGQAPGFSYTEANKNKGIIWGEQTLMEYLENPKKYIPGTKMIFAGLKKKSEREDLIEYLKQATSS
Mouse-T   GDAEAGKKIFVQKCAQCHTVEKGGKHKTGPNLWGLFGRKTGQAPGFSYTDANKNKGVIWSEETLMEYLENPKKYIPGTKTIFAGIKKKSEREDLIKYLKQATSS
Rat-T     GDAEAGKKIFIQKCAQCHTVEKGGKHKTGPNLWGLFGRKTGQAPGFSYTDANKNKGVIWTEETLMEYLENPKKYIPGTKMIFAGIKKKSEREDLIQYLKEATSS
```

Supplemental Figure 1A. Alignment of mammalian somatic (top) and testes (T, bottom) Cyt*c* sequences. Conserved amino acids are highlighted in yellow. Thr28 is highlighted in bold print. Accession numbers: NP_061820 (human); NP_001157486 (horse); NP_001039526 (cow); NP_001123442 (pig); NP_001183974 (dog); CAA25899 (mouse); NP_036971 (rat); EPQ18492 (bat); AJF48831 (goat); AFN27378 (dolphin); AAI02715 (bull testes); AAH59728 (mouse testes); NP_036972 (rat testes).

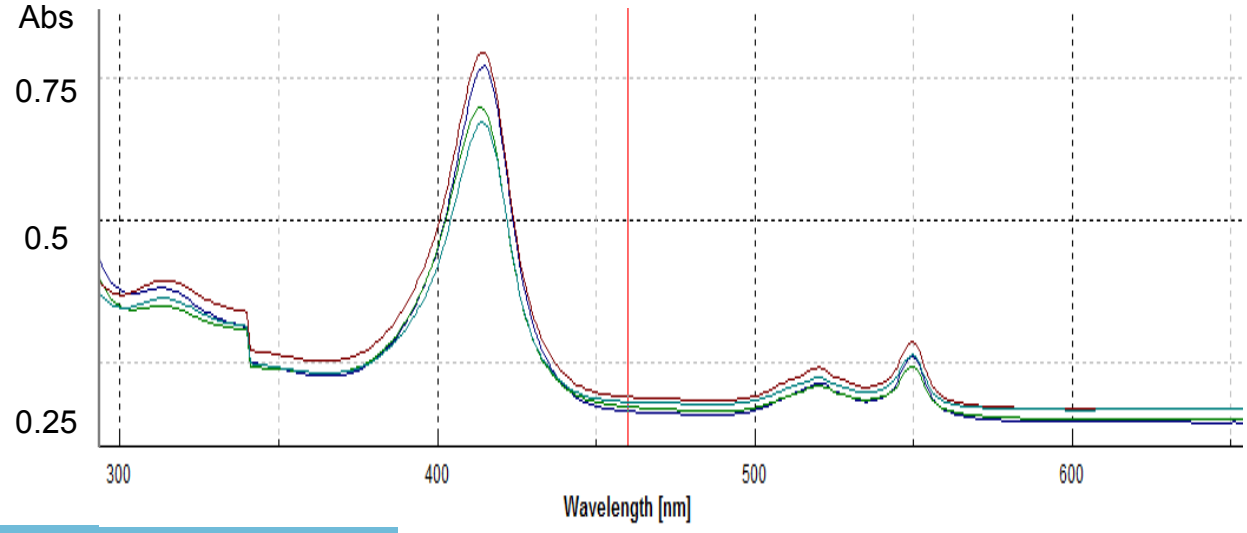

Supplemental Figure 1B. Spectral analysis of overexpressed and purified reduced WT (blue), Thr28Ala (green), Thr28Glu (red), and cow heart Sigma Cyt*c* as control (cyan) indicates correct folding and functionality of the proteins.

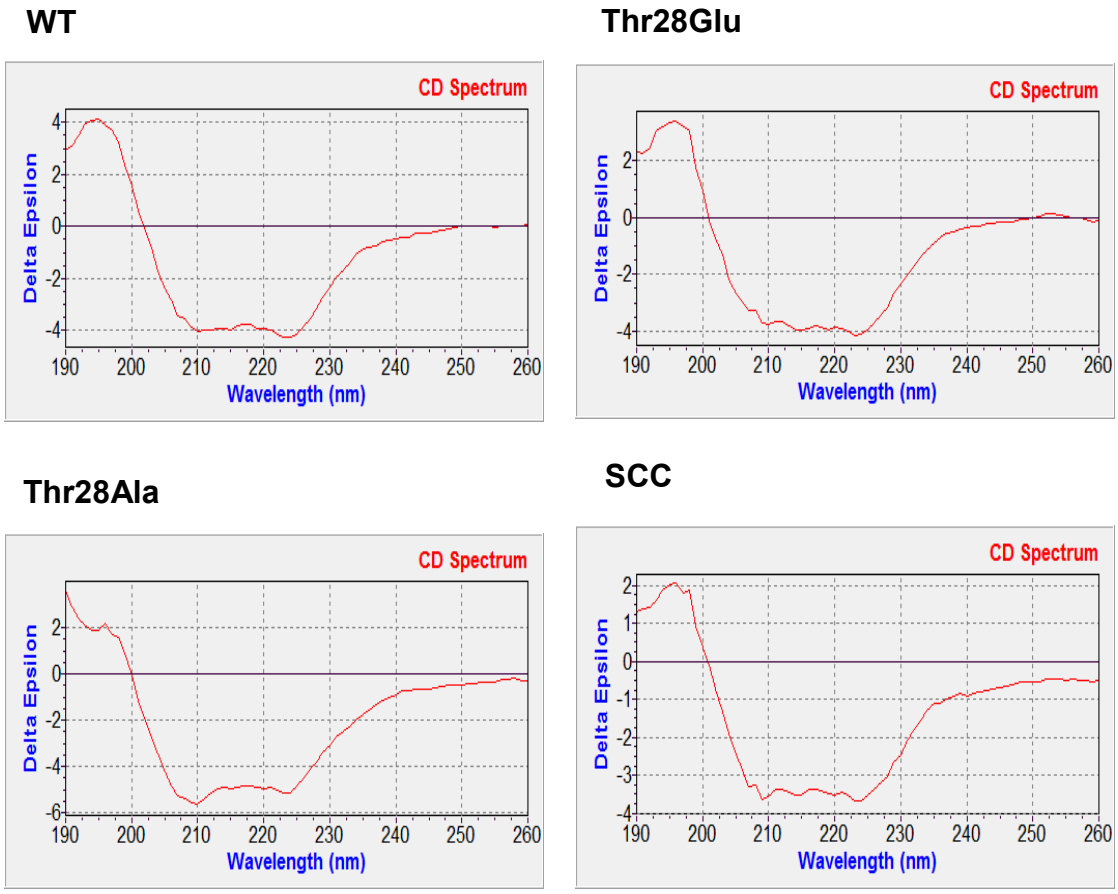

Supplemental Figure 1C. Circular dichroism spectra are similar for WT, Thr28Glu, and Sigma Cytc (SCC), whereas the Thr28Ala mutant shows spectral differences as lower wavelengths.

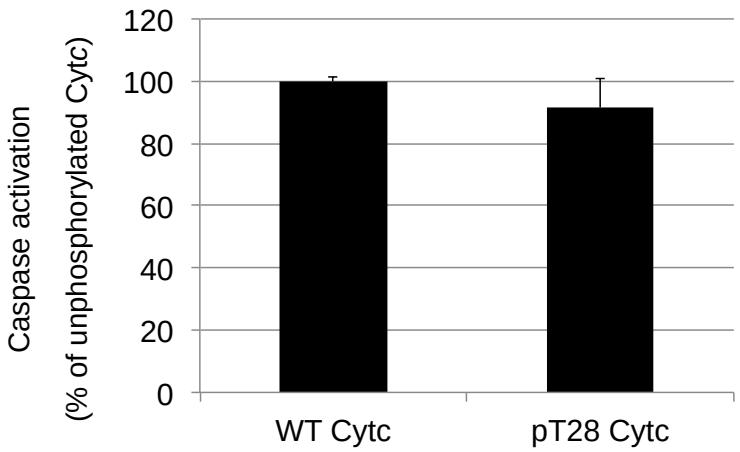

Supplemental Figure 2. Unphosphorylated (WT) and in vivo phosphorylated (pT28) Cyt*c* have a similar ability to induce caspase 3 activation in a cell free caspase assay.

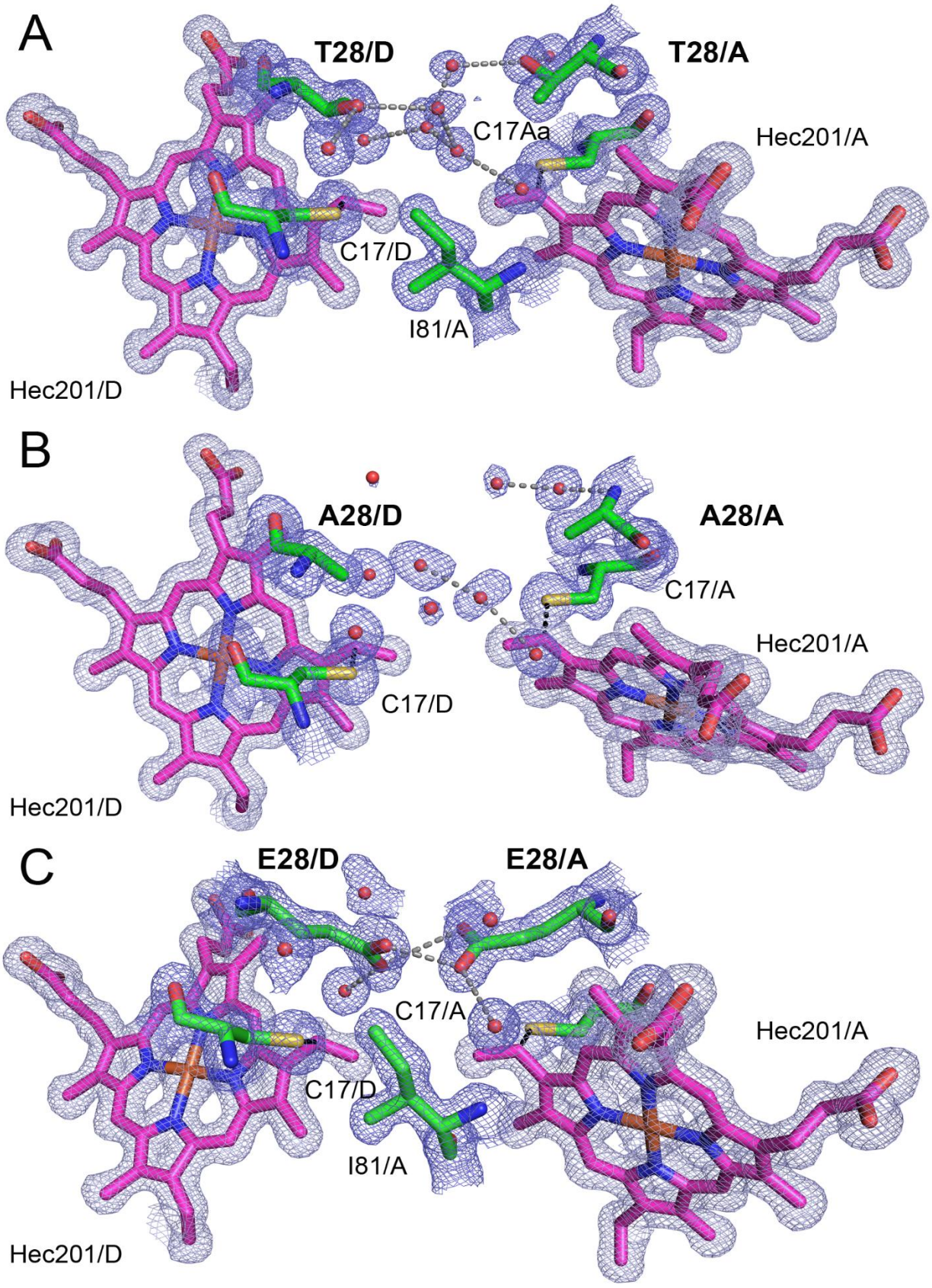

Supplemental Figure 3.

(A) Residues and water molecules near Thr28 in the WT protein (green carbon atoms) are shown with their electron density contoured at one sigma. To minimize the effects of differing side chain lengths and to make this figure for WT comparable to those for T28A and T28E, it includes all groups within 4 Å of Glu28 superposed onto Thr28. The heme (PDB code Hec) groups have magenta carbon atoms for contrast. The covalent links from Cys17 SG to the Hec vinyl groups (see Supplemental Table 1) are shown as black dashes. Hydrogen bonds are indicated with gray dashed lines.

(B) Equivalent to (A) above but for the T28A structure (5C9M.pdb), residues and water molecules near Ala28 (green carbon atoms) are shown with their electron density contoured at one sigma. To make this figure for T28A comparable to those for WT and T28E, it includes all groups within 4 Å of Glu28 superposed onto Ala28. Ile81/A, which is shown in Fig. 3xA and 3xC is omitted here because it was 4.1 Å from Glu28 in the superposed structure of T28E.

(C) Equivalent to A above but for the T28E structure (5DF5.pdb), residues and water molecules within 4Å of Glu28 (green carbon atoms) are shown with their electron density contoured at one sigma. The terminal oxygen atoms of the two Glu28 residues share two hydrogen bonds (2.72 & 3.25 Å) and are presumed to be protonated.

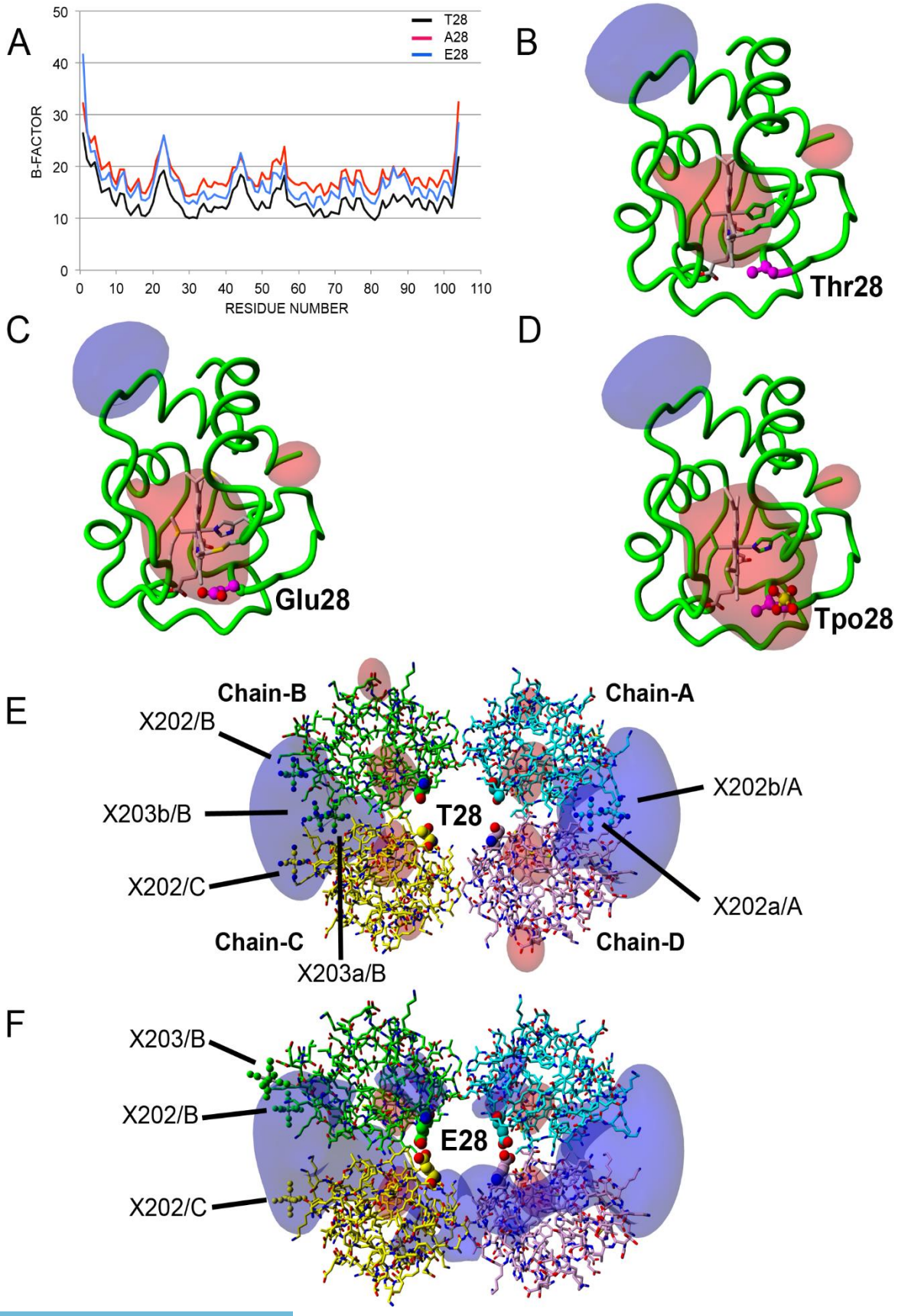

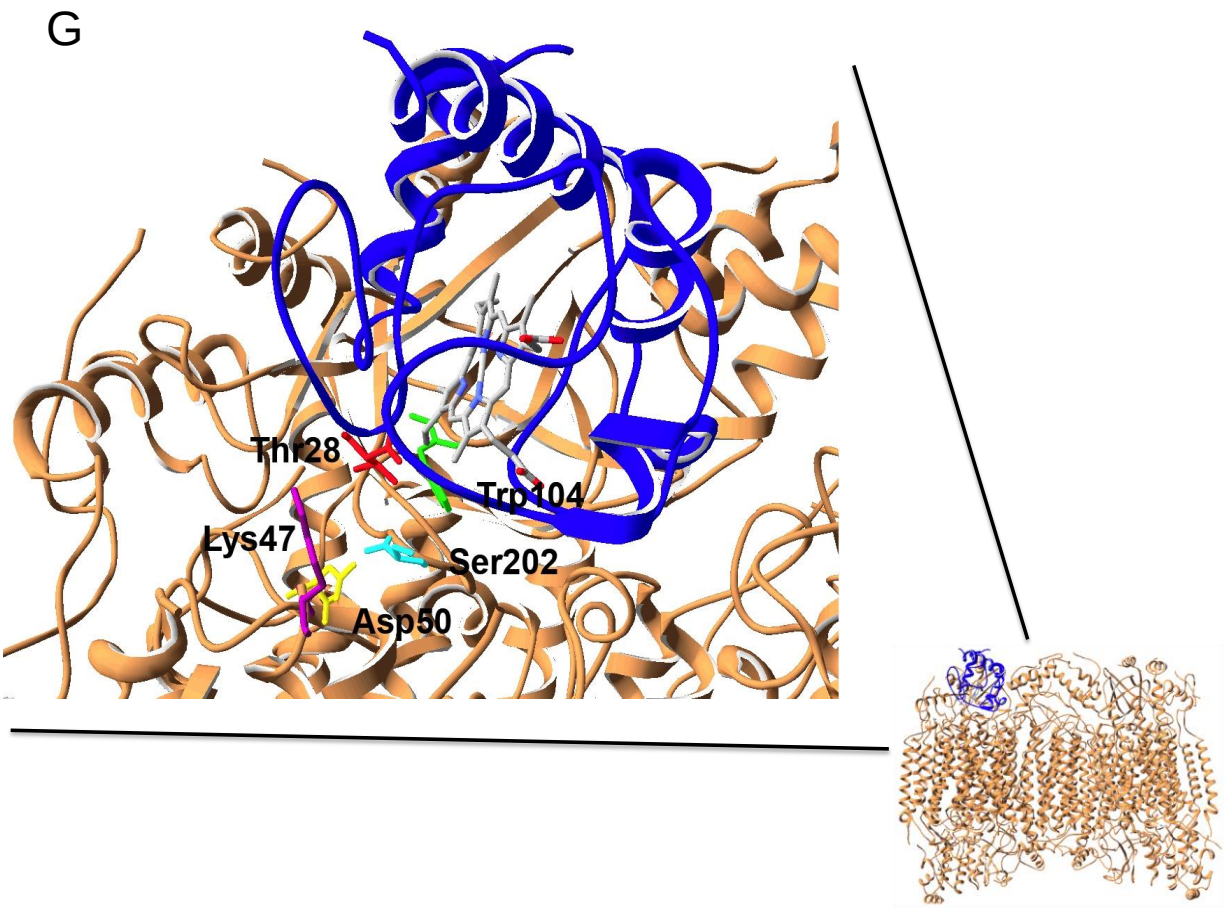

Supplemental Figure 4.

(A) Average B-Factors. The average temperature factor (B-factor) for the main chain atoms in WT (black), Thr28Ala (red), and Thr28EGlu (blue) are shown plotted by residue position.

(B) The negative (red) and positive (blue) electrostatic potential (ESP) are shown contoured at 20 kcal/mole for the WT protein shown as a “tube” tracing. The side chain atoms (magenta) of Thr28 are shown as balls. The ESP was calculated by YASARA using the recommended Nova force field *in vacuo* at pH 7.4. The ESP plot for the T28A mutant (not shown) is indistinguishable from this figure.

(C) The negative (red) and positive (blue) electrostatic potential (ESP) are shown contoured at 20 kcal/mole for the T28E mutant shown as a “tube” tracing. The side chain atoms (magenta) of Glu28 are shown as balls. The ESP was calculated by YASARA using the recommended Nova force field *in vacuo* at pH 7.4.

(D) The negative (red) and positive (blue) electrostatic potential (ESP) are shown contoured at 20 kcal/mole for the phosphor-Thr model (Tpo28) shown as a “tube” tracing. The side chain atoms (magenta) of Tpo28 are shown as balls. The ESP was calculated by YASARA using the recommended Nova force field *in vacuo* at pH 7.4.

(E) The entire WT "tetramer" in the unit cell of space group P1 is shown with its six hexacyanoferrate(3-) ligands (PDB code FC6) identified with "X" as a one letter code in this figure. X202a&b/A and X203a&b/B are pairs of FC6 ligands with partial occupancies and alternate positions (Supplemental Table 1) that physically overlap with each other and cannot be occupied simultaneously. The ESP was calculated by YASARA using the recommended Nova force field *in vacuo* at pH 7.4. The T28A tetramer, which is not shown, was crystallized under the same conditions as the WT protein, and has very similar FC6 ligands (Supplemental Table 1) and the same ESP contours.

(F) The entire T28E "tetramer" in the unit cell of space group P1 is shown with its three hexacyanoferrate(3-) ligands (PDB code FC6) identified with "X" as a one letter code. The ESP was calculated by YASARA using the recommended Nova force field *in vacuo* at pH 4.5. Given the close proximity and presumed hydrogen bonding between pairs of Glu28 residues (Supplemental Figure 3C) their pKa values were manually set to 7.0 so they would be protonated during the calculation of the ESP.

(G) Docking model of Cyt*c* and C*c*O [12]. Residues on C*c*O within a distance of 7 Å from Thr28 (red) are highlighted (Lys47 of C*c*O subunit 7c, magenta; Asp50 of C*c*O subunit I, yellow; Trp 104, green, and Ser 202, cyan, of C*c*O subunit II).

Supplemental Table 1. Crystallographic Data[1]

STRUCTURE	CYT*C* (WT) MOUSE	CYT*C* (T28A) MOUSE	CYT*C* (T28E) MOUSE	CYT*C* (Y47F) HUMAN[2]
PDB CODE	5C0Z	5C9M	5DF5	3ZOO
CRYSTALLIZATION				
Iron	Oxidized	Oxidized	Oxidized	Oxidized
Protein	15 mg/mL Cyt*c* (WT) + 5 mM	22 mg/mL Cyt*c* (T28A) + 5 mM	15 mg/mL Cyt*c* (T28E) + 5 mM	12.5 mg/mL oxidized protein in 22.5% (w/v)

	$K_3Fe(CN)_6$ in water	$K_3Fe(CN)_6$ in water	$K_3Fe(CN)_6$ in water	PEG 1000, 50 mM KH_2PO_4, pH 7.0
Well	25% PEG 4K, 8% isopropanol, 0.1 M Na acetate, pH 6.5	25% PEG 4K, 8% isopropanol, 0.1 M Na acetate, pH 6.5	30% PEG 1500, pH 4.5	26-31% (W/V) PEG 1000, 40 mM, KH_2PO_4 pH 7.0
Drop	1:1 protein:well	1:1 protein:well	1:1 protein:well	n/a
Cryoprotectant	30% PEG 4K, 8% iso propanol, 0.1M Na acetate, 20% ethylene glycol, 10 min soak with 5 mM $K_3Fe(CN)_6$	30% PEG 4K, 8% iso propanol, 0.1 M Na acetate, 20% ethylene glycol, 10 min soak with 5 mM $K_3Fe(CN)_6$	35% PEG 1500, 20% ethylene glycol	26-31% (w/v) PEG 1000, 40 mM, KH_2PO_4 pH 7.0, 15% glycerol
CRYSTAL DATA				
Space group:	P1	P1	P1	P1
Unit cell: a	34.401	34.517	34.609	36.367
b	52.471	52.567	51.739	53.952
c	61.647	61.771	61.748	58.95

Alpha	110.04	109.86	110.01	76.55
Beta	92.77	92.93	93.09	88.73
Gamma	92.02	92.20	91.88	71.86
Chains per A.U.	4	4	4	4
Matthews Coeff.	2.24	2.27	2.25	2.3
Solvent %	45.12	45.7	45.26	46.7
X-RAY DATA				
Resolution-high (Å)	1.124	1.36	1.30	1.35
Resolution-low (Å)	49.22	57.96	57.88	30.59
Beamline	APS 21-ID-F	APS 21-ID-F	APS 21-ID-D	DIAMOND 103 (UK)
Wavelength	0.97872	0.97872	1.07812	0.9762
Reflections	127840	76544	90455	81707
Completeness	87.4 (44.66)	92.4 (66.2)	96.6 (89.38)	94.73 (80.71)

Average I/sigma	14.4 (2.0)	14.1 (2.2)	14.9 (2.4)	8.70 (n/a)
Redundancy	3.9 (3.7)	3.9 (3.8)	5.3 (4.2)	n/a
Rmerge	0.05	0.052 (0.580)	0.081 (0.504)	0.07
REFINEMENT				
Rfactor	0.132 (0.239)	0.129 (0.229)	0.148 (0.256)	0.13821
Rfree	0.159 (0.240)	0.170 (0.303)	0.178 (0.252)	0.17935
Avg. B-factor (Å²)	15.97	21.41	19.32	17.703
Protein atoms per A.U.	3228	3220	3236	3981
Water molecules	537	472	334	417
Bond RMSD	0.017	0.016	0.018	0.017
Angle RMSD	1.903	1.803	1.884	1.99
Chiral RMSD	0.124	0.122	0.131	0.125
FC6 OCCUPANCY				

202a/A	0.28	0.35	–	
202b/A	0.37	0.34	–	
202/B	0.93	0.98	0.92	
203/B	–	–	0.48	
203a/B	0.30	0.39	–	
203b/B	0.32	0.28	–	
202/C	0.90	1.00	0.89	
HEME LINKS:				
C14 SG - HEM CAB (Å)				
Chain-A	1.86	1.92	1.91	1.93
Chain-B	1.86	1.93	1.90	1.96
Chain-C	1.91	1.94	1.95	1.96
Chain-D	1.95	2.02	1.94	1.93
Average	1.90	1.95	1.93	1.95
C17 SG - HEM CAC (Å)				
Chain-A	1.98	2.09	1.96	2.06

Chain-B	1.94	2.07	1.99	2.21
Chain-C	1.97	2.12	2.07	2.16
Chain-D	2.04	2.21	2.06	2.08
Average	**1.98**	**2.12**	**2.02**	**2.13**
H18 NE2 - FE2 (Å)				
Chain-A	2.02	2.03	2.00	2.00
Chain-B	2.03	2.00	2.02	2.06
Chain-C	2.02	2.04	2.03	2.01
Chain-D	2.01	2.07	2.02	2.02
Average	**2.02**	**2.04**	**2.02**	**2.02**
M80 SD - FE2 (Å)				
Chain-A	2.29	2.27	2.28	2.29
Chain-B	2.28	2.27	2.27	2.29
Chain-C	2.30	2.28	2.30	2.24
Chain-D	2.31	2.27	2.29	2.29
Average	**2.30**	**2.27**	**2.29**	**2.28**

[1]All three structures have 4 molecules in a P1 unit cell with very similar dimensions. When the twelve independently refined Cytc molecules are overlapped with each other using their main chain atoms, the average RMSD value among the 66 unique pairs is 0.189 Å, and the highest value is 0.280 Å between chain-A in WT and chain-D in Thr28Glu. Comparing equivalent chains, the three A-chains have the smallest RMSD (0.080 Å) followed by the B-chains (0.107 Å), the D-chains (0.0.113 Å) and the C-chains (0.140 Å). The three Cyt*c* "tetramers" reported here have a similar orientation in the P1 unit cell. The Thr28Ala and Thr28Glu mutants have RMSD values, based on backbone atoms, of 0.151 Å and 0.330 Å, respectively, when superposed on the WT structure as tetramers. The Thr28Ala structure is more similar to the WT structure because it was crystallized at pH 6.5 from the exact same conditions as the WT protein, whereas the Thr28Glu mutant was crystallized from a different solution at pH 4.5. The Thr28Glu mutant only crystallized at pH 4.5 because the four Glu28 residues, are arranged in closely adjacent pairs in the "native" tetramer and destabilizes the crystal packing if they are deprotonated (see Supplemental Figures 3 and 4). The Thr28Glu crystal structure has the same two major FC6 ligands (FC6 202/B and FC6/C), as the WT structure and a third, unique site (FC6 203/B), which is possibly related to the lower pH. It has no significant density for the two minor sites (FC6 202/A and FC6 203/B) in the WT and Thr28Ala crystal structures. The lower occupancies of the minor FC6 sites suggest they are weakly bound and were probably lost from the Thr28Glu crystals during the crystal freezing procedure, which used a cryo-solution soak that did not include the FC6 reagent.

[2]Mouse and human Cyt*c* monomers are similar but their tetramers differ: The mouse WT structure was solved using chain-A from the crystal structure of human Cyt*c* (see Methods), and the two refined chains have a RMSD of 0.266. Also, the three mouse structures, like the human structure, were solved and refined using the free heme moiety (PDB ligand code: HEM) and finished with very similar, unconstrained bond distances for the dative bonds to heme iron and the covalent links to Cys14 and Cys17. In contrast, the tetramers observed in both crystal structures, have a RMSD overlap of 17 Å because the Cyt*c* molecules have very different orientations within the tetramer (not shown). The tetramers are crystal entities and do not exist in solution. All three Cyt*c* monomers – WT, Thr28Ala, Thr28Glu – have a region with strong positive electrostatic potential (ESP) (Supplemental Figure 4E and F). In the three structures reported here, the monomers are arranged with their positive ESP regions adjacent to each other in pairs. This arrangement is possible because the FC6 ligands with their -3 charge balance the strong positive ESP. The human Cyt*c* lacks these ligands. Consequently, the monomers are rotated within the human tetramer so the ESP potentials are distant from each other (not shown).

CHAPTER 3 SUMMARY

To understand how Cyt*c* phosphorylation is induced under stressed conditions, and how it functions in protecting tissues affected by that stress, we performed a second study where the phosphorylation status of Cyt*c* in ischemic brain was investigated. The following article demonstrates how insulin-induced neuroprotection and inhibition of Cyt*c* release under conditions of brain ischemia was connected to Cyt*c* phosphorylation. Our data suggest that phosphorylation of Cyt*c* occurs in an insulin-dependent manner, and significantly reduces induction of apoptosis via prevention of Cyt*c* release from mitochondria (manuscript published in PLoS One, 2013 8(11):e78627).

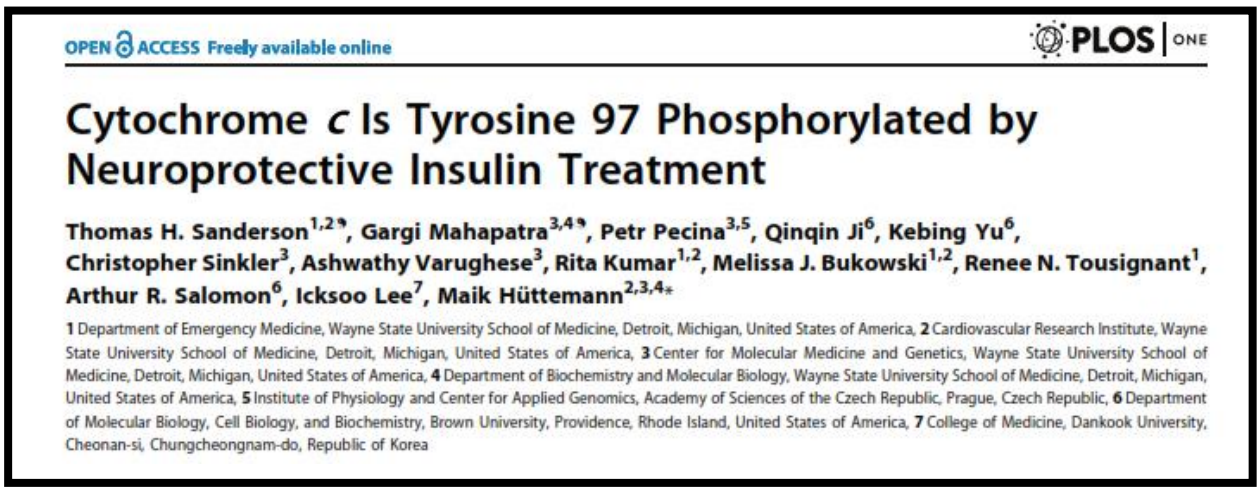

OPEN ACCESS Freely available online

PLOS | ONE

Cytochrome *c* Is Tyrosine 97 Phosphorylated by Neuroprotective Insulin Treatment

Thomas H. Sanderson[1,2☯], Gargi Mahapatra[3,4☯], Petr Pecina[3,5], Qinqin Ji[6], Kebing Yu[6], Christopher Sinkler[3], Ashwathy Varughese[3], Rita Kumar[1,2], Melissa J. Bukowski[1,2], Renee N. Tousignant[1], Arthur R. Salomon[6], Icksoo Lee[7], Maik Hüttemann[2,3,4]*

1 Department of Emergency Medicine, Wayne State University School of Medicine, Detroit, Michigan, United States of America, **2** Cardiovascular Research Institute, Wayne State University School of Medicine, Detroit, Michigan, United States of America, **3** Center for Molecular Medicine and Genetics, Wayne State University School of Medicine, Detroit, Michigan, United States of America, **4** Department of Biochemistry and Molecular Biology, Wayne State University School of Medicine, Detroit, Michigan, United States of America, **5** Institute of Physiology and Center for Applied Genomics, Academy of Sciences of the Czech Republic, Prague, Czech Republic, **6** Department of Molecular Biology, Cell Biology, and Biochemistry, Brown University, Providence, Rhode Island, United States of America, **7** College of Medicine, Dankook University, Cheonan-si, Chungcheongnam-do, Republic of Korea

CHAPTER 4 CONCLUSIONS AND FUTURE DIRECTIONS

This dissertation set out to investigate the role Cyt*c* phosphorylation plays in various aspects of life, under physiologically healthy and stressed conditions, and to use biochemical and molecular biological techniques to decipher the mechanisms affected by it. In this final chapter, I will review the research contributions of this dissertation, as well as discuss directions for future research.

4.1 Conclusions

The importance of cell signaling pathways in regulating protein functions have been known for many years. Mitochondrial proteins have been known to be post-translationally modified, altering their functions under influence from cell-signaling pathways targeting them. The understanding of how phosphorylation of mitochondrial electron transport chain (ETC) protein Cyt*c* function is naturally of great importance and was the main motivation for this thesis. The work consisted of three parts: discovering the amino acid residue that are endogenously phosphorylated on Cyt*c* under physiologically healthy conditions in tissues like kidneys and brain, the effect of these phosphorylations on the functioning of the protein, for example control of the rate of reduction, and the transfer of electrons between complexes III and IV of the ETC, and discovering the kinase(s) that are responsible for the phosphorylations on the protein. As models for our study, the following proteins were used: the wild-type rat Cyt*c* protein, the phosphomimetic Thr28Glu Cytc mutant, and the non-phosphorylatable Thr28Ala Cyt*c* (an additional control). This thesis research has contributed incremental but significant results for the continuing study of phosphorylated mitochondrial proteins, and some suggestions for further work. Multiple studies from our laboratory showed that Cyt*c* is tightly regulated

by post-translational modifications, especially phosphorylation. Site-specific phosphorylations on Cyt*c* were discovered in our laboratory with the help of techniques of purification of the protein that helps in preserving the physiological phosphorylation status of the protein, as it was present within the healthy live tissue. Cyt*c* was previously isolated from mammalian heart and liver tissues in our laboratory and site specific tyrosine phosphorylations were detected by Nano/LC/ESI/MS/MS. Experiments showed that these phosphorylations had significant impact on the various functions of the protein, proving that phosphorylation of the protein is undoubtedly important. These results led to our overall hypothesis that Cyt*c* phosphorylation does regulate the two major functions of Cyt*c*, mitochondrial respiration and Cyt*c* release during apoptosis. The long term goal of our laboratory is therefore to understand the effect of Cyt*c* phosphorylation on respiration and apoptosis, and to identify the cell signaling pathways directed to Cyt*c*.

This thesis research aimed at understanding Cyt*c* phosphorylation in detail, by investigating the project via addressing three specific aims: 1) testing the hypotheses that Cyt*c* is in vivo phosphorylated under physiologically healthy conditions in a distinct tissue-specific manner, 2) testing the hypotheses that phosphorylation of Cyt*c* leads to controlled respiration and prevents its participation in activation of the Cyt*c*-mediated apoptosis cascade, and 3) to systematically identify mitochondrial kinases that phosphorylate Cyt*c* on specific residues in a tissue-specific manner. Whether these phosphorylations result in structural changes of the protein is under study. This thesis research discloses that the long recognized central molecule in respiration and apoptosis, Cyt*c*, is regulated by cell signaling pathways that target mitochondria under healthy conditions, opening new avenues to understand and control the two main biological processes that depend totally

on this small single electron carrier protein. In a follow-up study, we are analyzing whether there are any structural changes brought about by site-specific phosphorylation, and identify the kinases and phosphatases that phosphorylate and dephosphorylate Cyt*c*. Since Cyt*c*-mediated apoptosis and cellular respiration play a crucial role in many diseases such as cancer and neurodegeneration, this study is anticipated to provide better understanding and control of such diseases.

Cell signaling pathways that target the mitochondria are not well defined and are poorly understood. Major metabolic regulators that are known to affect mitochondrial functions, such as insulin, glucagon, and calcium, have not been well studied to reveal their mechanism of action. However, our laboratory has published protocols to isolate mitochondria and ETC components which preserve their endogenous phosphorylation state, and we provide compelling evidence that cell signaling pathways act on Cyt*c* in a distinct and tissue-specific manner. During this thesis research, we developed methods to assess the levels of endogenous Cyt*c* phosphorylation, and for the first time, we identified the kinase that phosphorylates Cyt*c* in kidney tissues under healthy conditions, phosphorylating Cyt*c* at Thr28 residue. We show that it is the AMP-kinase-mediated phosphorylated form of Cyt*c* that exists in healthy kidney tissues in vivo, and functional studies revealed that phosphorylation on this site leads to controlled respiration, reduced cardiolipin peroxidase activity, which is required for its release from the mitochondria during apoptosis, and unaltered capability to induce caspase activation with Thr28 phosphomimetic Cyt*c*. This research indicates that Thr28 site is important in the redox-functioning of the protein, and plays an important role in maintain the native structure and

functions of the protein under healthy conditions, when the protein resides within the mitochondrial intermembrane space.

4.2 Future directions

To further advance our understanding of how phosphorylation of Cyt*c* affected its functions under physiological conditions, several steps can be taken to address questions that arise with this research.

4.2.1 How to better study tissue-specific phosphorylations?

Tissue-specific phosphorylations can be better studied by approaching to study tissue-specific phosphorylations by creating animal models expressing phosphomimetic Cyt*c* in individual sites in tissues that they were discovered in, and comparing them with wild type Cyt*c* expressing animals. This will address multiple questions at the same time. We will be able to find out how the phosphorylation of the protein alters the animal's ability to survive conditions which are stressful under physiological conditions.

Second, to discover the level and sites that are physiologically phosphorylated in different tissues within one healthy animal, purification of Cyt*c* can be performed followed by mass spectrometry. This would give an overall understanding of the phosphorylations that exist in a healthy animal at a time, in different tissues. Then, changes in the phosphorylation profiles in different tissues could be studied under different stressed conditions. Also, changes in the protein functions can also be measured by various assays that has been performed in this thesis project. Changes in cellular activities could also be monitored by isolation of primary cells and/or intact mitochondria from various tissues under different conditions. This would signify how Cyt*c*

phosphorylation maintains healthy conditions of tissues and how it is affected by stress, thereby affecting the protein's functions.

Third, if more than one site is phosphorylated in the protein purified from the same tissue, then double as well as single phospho-mimetic mutant proteins can be prepared, and the activities can be compared to one another, as well as the wild type protein. This will suggest if phosphorylation on one particular site lead to altered activities or if it is a combination of all the existing phosphorylations.

Fourth, deciphering the different kinases and phosphatases within the mitochondrial intermembrane space targeting the Cyt*c* protein and phosphorylating it on different sites will suggest the combination of signaling pathways that converge on mitochondria of a specific tissue at a time, and result in Cyt*c* phosphorylation. Experiments performed to find out if any one site affected the protein's function more than the other will indicate which signaling pathway has a stronger impact on mitochondrial functions through Cyt*c* phosphorylation.

Fifth, to follow changes in phosphorylation status of Cyt*c* under various stressful conditions, antibodies can be raised against Cyt*c* phosphorylated at a particular site. These phospho-site-specific antibodies can be used to track changes in the levels of phosphorylation on the particular site within tissue-sections or purified proteins.

REFERENCES

1 Lee, I. *et al.* New prospects for an old enzyme: mammalian cytochrome c is tyrosine-phosphorylated in vivo. *Biochemistry* **45**, 9121-9128, doi:10.1021/bi060585v (2006).

2 Ow, Y. P., Green, D. R., Hao, Z. & Mak, T. W. Cytochrome c: functions beyond respiration. *Nature reviews. Molecular cell biology* **9**, 532-542, doi:10.1038/nrm2434 (2008).

3 Brown, G. C. & Borutaite, V. Regulation of apoptosis by the redox state of cytochrome c. *Biochim Biophys Acta* **1777**, 877-881, doi:10.1016/j.bbabio.2008.03.024 (2008).

4 Salemme, F. R. Structure and function of cytochromes c. *Annu. Rev. Biochem.* **46**, 299-329, doi:10.1146/annurev.bi.46.070177.001503 (1977).

5 Orrenius, S. & Zhivotovsky, B. Cardiolipin oxidation sets cytochrome c free. *Nature chemical biology* **1**, 188-189, doi:10.1038/nchembio0905-188 (2005).

6 Margoliash, E. The Amino Acid Sequence of Cytochrome C in Relation to Its Function and Evolution. *Canadian journal of biochemistry* **42**, 745-753 (1964).

7 Huttemann, M., Jaradat, S. & Grossman, L. I. Cytochrome c oxidase of mammals contains a testes-specific isoform of subunit VIb--the counterpart to testes-specific cytochrome c? *Molecular reproduction and development* **66**, 8-16, doi:10.1002/mrd.10327 (2003).

8 Slater, E. C. Keilin, cytochrome, and the respiratory chain. *The Journal of biological chemistry* **278**, 16455-16461, doi:10.1074/jbc.X200011200 (2003).

9 Dickerson, R. E., Kopka, M. L., Borders, C. L., Jr., Varnum, J. & Weinzier, J. E. A centrosymmetric projection at 4A of horse heart oxidized cytochrome c. *J. Mol. Biol.* **29**, 77-95 (1967).

10 Bushnell, G. W., Louie, G. V. & Brayer, G. D. High-resolution three-dimensional structure of horse heart cytochrome c. *J. Mol. Biol.* **214**, 585-595, doi:10.1016/0022-2836(90)90200-6 (1990).

11 Lange, C. & Hunte, C. Crystal structure of the yeast cytochrome bc1 complex with its bound substrate cytochrome c. *Proc. Natl. Acad. Sci. U. S. A.* **99**, 2800-2805, doi:10.1073/pnas.052704699 (2002).

12 Roberts, V. A. & Pique, M. E. Definition of the interaction domain for cytochrome c on cytochrome c oxidase. III. Prediction of the docked complex by a complete, systematic search. *J. Biol. Chem.* **274**, 38051-38060 (1999).

13 Waldmeyer, B., Bechtold, R., Bosshard, H. R. & Poulos, T. L. The cytochrome c peroxidase.cytochrome c electron transfer complex. Experimental support of a hypothetical model. *The Journal of biological chemistry* **257**, 6073-6076 (1982).

14 Poulos, T. L. & Kraut, J. A hypothetical model of the cytochrome c peroxidase . cytochrome c electron transfer complex. *The Journal of biological chemistry* **255**, 10322-10330 (1980).

15 Li, K. *et al.* Cytochrome c deficiency causes embryonic lethality and attenuates stress-induced apoptosis. *Cell* **101**, 389-399 (2000).

16 Hakem, R. *et al.* Differential requirement for caspase 9 in apoptotic pathways in vivo. *Cell* **94**, 339-352 (1998).

17 Vaux, D. L. & Korsmeyer, S. J. Cell death in development. *Cell* **96**, 245-254 (1999).

18 Acin-Perez, R. *et al.* An intragenic suppressor in the cytochrome c oxidase I gene of mouse mitochondrial DNA. *Hum. Mol. Genet.* **12**, 329-339 (2003).

19 Dalmonte, M. E. *et al.* Control of respiration by cytochrome c oxidase in intact cells: role of the membrane potential. *J. Biol. Chem.* **284**, 32331-32335, doi:10.1074/jbc.M109.050146 (2009).

20 Piccoli, C., Scrima, R., Boffoli, D. & Capitanio, N. Control by cytochrome c oxidase of the cellular oxidative phosphorylation system depends on the mitochondrial energy state. *Biochem. J.* **396**, 573-583, doi:10.1042/BJ20060077 (2006).

21 Villani, G. & Attardi, G. In vivo control of respiration by cytochrome c oxidase in wild-type and mitochondrial DNA mutation-carrying human cells. *Proc. Natl. Acad. Sci. U. S. A.* **94**, 1166-1171 (1997).

22 Villani, G., Greco, M., Papa, S. & Attardi, G. Low reserve of cytochrome c oxidase capacity in vivo in the respiratory chain of a variety of human cell types. *J. Biol. Chem.* **273**, 31829-31836 (1998).

23 Hinkle, P. C., Kumar, M. A., Resetar, A. & Harris, D. L. Mechanistic stoichiometry of mitochondrial oxidative phosphorylation. *Biochemistry* **30**, 3576-3582 (1991).

24 Dumont, M. E., Cardillo, T. S., Hayes, M. K. & Sherman, F. Role of cytochrome c heme lyase in mitochondrial import and accumulation of cytochrome c in Saccharomyces cerevisiae. *Mol. Cell. Biol.* **11**, 5487-5496 (1991).

25 Riemer, J., Fischer, M. & Herrmann, J. M. Oxidation-driven protein import into mitochondria: Insights and blind spots. *Biochim. Biophys. Acta* **1808**, 981-989, doi:10.1016/j.bbamem.2010.06.003 (2011).

26 Chacinska, A. *et al.* Essential role of Mia40 in import and assembly of mitochondrial intermembrane space proteins. *Embo J* **23**, 3735-3746 (2004).

27 Allen, S., Balabanidou, V., Sideris, D. P., Lisowsky, T. & Tokatlidis, K. Erv1 mediates the Mia40-dependent protein import pathway and provides a functional link to the respiratory chain by shuttling electrons to cytochrome c. *J. Mol. Biol.* **353**, 937-944, doi:10.1016/j.jmb.2005.08.049 (2005).

28 Cadenas, E. & Davies, K. J. Mitochondrial free radical generation, oxidative stress, and aging. *Free Radic. Biol. Med.* **29**, 222-230 (2000).

29 Kadenbach, B., Arnold, S., Lee, I. & Huttemann, M. The possible role of cytochrome c oxidase in stress-induced apoptosis and degenerative diseases. *Biochim. Biophys. Acta* **1655**, 400-408, doi:10.1016/j.bbabio.2003.06.005 (2004).

30 Korshunov, S. S., Krasnikov, B. F., Pereverzev, M. O. & Skulachev, V. P. The antioxidant functions of cytochrome c. *FEBS Lett.* **462**, 192-198 (1999).

31 Pereverzev, M. O., Vygodina, T. V., Konstantinov, A. A. & Skulachev, V. P. Cytochrome c, an ideal antioxidant. *Biochem Soc Trans* **31**, 1312-1315 (2003).

32 Wang, Z. B., Li, M., Zhao, Y. & Xu, J. X. Cytochrome C is a hydrogen peroxide scavenger in mitochondria. *Protein and peptide letters* **10**, 247-253 (2003).

33 Nemoto, S. *et al.* The mammalian longevity-associated gene product p66shc regulates mitochondrial metabolism. *J. Biol. Chem.* **281**, 10555-10560, doi:10.1074/jbc.M511626200 (2006).

34 Giorgio, M. *et al.* Electron transfer between cytochrome c and p66Shc generates reactive oxygen species that trigger mitochondrial apoptosis. *Cell* **122**, 221-233 (2005).

35 Sun, L. *et al.* p66Shc mediates high-glucose and angiotensin II-induced oxidative stress renal tubular injury via mitochondrial-dependent apoptotic pathway. *Am. J. Physiol. Renal Physiol.* **299**, F1014-1025, doi:10.1152/ajprenal.00414.2010 (2010).

36 Liu, X., Kim, C. N., Yang, J., Jemmerson, R. & Wang, X. Induction of apoptotic program in cell-free extracts: requirement for dATP and cytochrome c. *Cell* **86**, 147-157 (1996).

37 Krippner, A., Matsuno-Yagi, A., Gottlieb, R. A. & Babior, B. M. Loss of function of cytochrome c in Jurkat cells undergoing fas-mediated apoptosis. *J. Biol. Chem.* **271**, 21629-21636 (1996).

38 Wang, X. The expanding role of mitochondria in apoptosis. *Genes Dev.* **15**, 2922-2933 (2001).

39 Jacobs, E. E. & Sanadi, D. R. The reversible removal of cytochrome c from mitochondria. *J. Biol. Chem.* **235**, 531-534 (1960).

40 Doran, E. & Halestrap, A. P. Cytochrome c release from isolated rat liver mitochondria can occur independently of outer-membrane rupture: possible role of contact sites. *Biochem. J.* **348 Pt 2**, 343-350 (2000).

41 Clayton, R., Clark, J. B. & Sharpe, M. Cytochrome c release from rat brain mitochondria is proportional to the mitochondrial functional deficit: implications for apoptosis and neurodegenerative disease. *J. Neurochem.* **92**, 840-849, doi:10.1111/j.1471-4159.2004.02918.x (2005).

42 Schlame, M., Rua, D. & Greenberg, M. L. The biosynthesis and functional role of cardiolipin. *Prog. Lipid Res.* **39**, 257-288 (2000).

43 Kagan, V. E. *et al.* Oxidative lipidomics of apoptosis: redox catalytic interactions of cytochrome c with cardiolipin and phosphatidylserine. *Free Radic. Biol. Med.* **37**, 1963-1985, doi:10.1016/j.freeradbiomed.2004.08.016 (2004).

44 Kagan, V. E. *et al.* Cytochrome c acts as a cardiolipin oxygenase required for release of proapoptotic factors. *Nat. Chem. Biol.* **1**, 223-232, doi:10.1038/nchembio727 (2005).

45 Nakagawa, Y. Initiation of apoptotic signal by the peroxidation of cardiolipin of mitochondria. *Ann. N. Y. Acad. Sci.* **1011**, 177-184 (2004).

46 Svistunenko, D. A. Reaction of haem containing proteins and enzymes with hydroperoxides: the radical view. *Biochim. Biophys. Acta* **1707**, 127-155, doi:10.1016/j.bbabio.2005.01.004 (2005).

47 Tyurina, Y. Y. *et al.* Mechanisms of cardiolipin oxidation by cytochrome c: relevance to pro- and antiapoptotic functions of etoposide. *Mol. Pharmacol.* **70**, 706-717, doi:10.1124/mol.106.022731 (2006).

48 Arnold, S. & Kadenbach, B. The intramitochondrial ATP/ADP-ratio controls cytochrome c oxidase activity allosterically. *FEBS Lett.* **443**, 105-108 (1999).

49 Ferguson-Miller, S., Brautigan, D. L. & Margoliash, E. Correlation of the kinetics of electron transfer activity of various eukaryotic cytochromes c with binding to mitochondrial cytochrome c oxidase. *J Biol Chem* **251**, 1104-1115 (1976).

50 Napiwotzki, J., Shinzawa-Itoh, K., Yoshikawa, S. & Kadenbach, B. ATP and ADP bind to cytochrome c oxidase and regulate its activity. *Biol. Chem.* **378**, 1013-1021 (1997).

51 Craig, D. B. & Wallace, C. J. Studies of 8-azido-ATP adducts reveal two mechanisms by which ATP binding to cytochrome c could inhibit respiration. *Biochemistry* **34**, 2686-2693 (1995).

52 Tuominen, E. K. *et al.* ATP induces a conformational change in lipid-bound cytochrome c. *J. Biol. Chem.* **276**, 19356-19362, doi:10.1074/jbc.M100853200 (2001).

53 Goldberg, E., Sberna, D., Wheat, T. E., Urbanski, G. J. & Margoliash, E. Cytochrome c: immunofluorescent localization of the testis-specific form. *Science* **196**, 1010-1012 (1977).

54 Hess, R. A., Miller, L. A., Kirby, J. D., Margoliash, E. & Goldberg, E. Immunoelectron microscopic localization of testicular and somatic cytochromes c in the seminiferous epithelium of the rat. *Biol. Reprod.* **48**, 1299-1308 (1993).

55 Liu, Z. *et al.* Remarkably high activities of testicular cytochrome c in destroying reactive oxygen species and in triggering apoptosis. *Proc Natl Acad Sci U S A* **103**, 8965-8970 (2006).

56 Zhang, Z. & Gerstein, M. The human genome has 49 cytochrome c pseudogenes, including a relic of a primordial gene that still functions in mouse. *Gene* **312**, 61-72 (2003).

57 Holzschu, D. *et al.* Replacement of the invariant lysine 77 by arginine in yeast iso-1-cytochrome c results in enhanced and normal activities in vitro and in vivo. *J. Biol. Chem.* **262**, 7125-7131 (1987).

58 Paik, W. K., Cho, Y. B., Frost, B. & Kim, S. Cytochrome c methylation. *Biochem. Cell Biol.* **67**, 602-611 (1989).

59 Farooqui, J., Kim, S. & Paik, W. K. In vivo studies on yeast cytochrome c methylation in relation to protein synthesis. *J. Biol. Chem.* **255**, 4468-4473 (1980).

60 Cessay, K. J., Bergman, L. W. & Tuck, M. T. Further investigations regarding the role of trimethyllysine for cytochrome c uptake into mitochondria. *Int. J. Biochem.* **23**, 761-768 (1991).

61 Kluck, R. M. *et al.* Determinants of cytochrome c pro-apoptotic activity. The role of lysine 72 trimethylation. *J. Biol. Chem.* **275**, 16127-16133 (2000).

62 Schonhoff, C. M., Gaston, B. & Mannick, J. B. Nitrosylation of cytochrome c during apoptosis. *J. Biol. Chem.* **278**, 18265-18270, doi:10.1074/jbc.M212459200 (2003).

63 Covian, R. & Balaban, R. S. Cardiac mitochondrial matrix and respiratory complex protein phosphorylation. *Am. J. Physiol. Heart Circ. Physiol.* **303**, H940-966, doi:10.1152/ajpheart.00077.2012 (2012).

64 Demory, M. L. *et al.* Epidermal growth factor receptor translocation to the mitochondria: regulation and effect. *J. Biol. Chem.* **284**, 36592-36604, doi:10.1074/jbc.M109.000760 (2009).

65 Helling, S. *et al.* Multiple phosphorylations of cytochrome c oxidase and their functions. *Proteomics* **12**, 950-959, doi:10.1002/pmic.201100618 (2012).

66 Huttemann, M., Lee, I., Grossman, L. I., Doan, J. W. & Sanderson, T. H. Phosphorylation of mammalian cytochrome c and cytochrome c oxidase in the regulation of cell destiny: respiration, apoptosis, and human disease. *Advances in experimental medicine and biology* **748**, 237-264, doi:10.1007/978-1-4614-3573-0_10 (2012).

67 Yu, H., Lee, I., Salomon, A. R., Yu, K. & Huttemann, M. Mammalian liver cytochrome c is tyrosine-48 phosphorylated in vivo, inhibiting mitochondrial respiration. *Biochimica et biophysica acta* **1777**, 1066-1071, doi:10.1016/j.bbabio.2008.04.023 (2008).

68 Pecina, P. *et al.* Phosphomimetic substitution of cytochrome C tyrosine 48 decreases respiration and binding to cardiolipin and abolishes ability to trigger downstream caspase activation. *Biochemistry* **49**, 6705-6714, doi:10.1021/bi100486s (2010).

69 Yu, T., Wang, X., Purring-Koch, C., Wei, Y. & McLendon, G. L. A mutational epitope for cytochrome C binding to the apoptosis protease activation factor-1. *J. Biol. Chem.* **276**, 13034-13038, doi:10.1074/jbc.M009773200 (2001).

70 Huttemann, M. *et al.* Regulation of oxidative phosphorylation, the mitochondrial membrane potential, and their role in human disease. *Journal of bioenergetics and biomembranes* **40**, 445-456, doi:10.1007/s10863-008-9169-3 (2008).

71 Sanderson, T. H. *et al.* Cytochrome c is tyrosine 97 phosphorylated by neuroprotective insulin treatment. *PLoS One* **8**, e78627, doi:10.1371/journal.pone.0078627 (2013).

72 Green, D. R. & Reed, J. C. Mitochondria and apoptosis. *Science* **281**, 1309-1312 (1998).

73 Lee, I. *et al.* New prospects for an old enzyme: mammalian cytochrome *c* is tyrosine-phosphorylated in vivo. *Biochemistry* **45**, 9121-9128 (2006).

74 Yu, H., Lee, I., Salomon, A. R., Yu, K. & Hüttemann, M. Mammalian liver cytochrome *c* is tyrosine-48 phosphorylated in vivo, inhibiting mitochondrial respiration. *Biochim Biophys Acta* **1777**, 1066-1071 (2008).

75 Pecina, P. *et al.* Phosphomimetic substitution of cytochrome c tyrosine 48 decreases respiration and binding to cardiolipin and abolishes ability to trigger downstream caspase activation. *Biochemistry* **49**, 6705-6714 (2010).

76 Kadenbach, B., Arnold, S., Lee, I. & Hüttemann, M. The possible role of cytochrome *c* oxidase in stress-induced apoptosis and degenerative diseases. *Biochim Biophys Acta* **1655**, 400-408 (2004).

77 Vempati, U. D. *et al.* Role of cytochrome C in apoptosis: increased sensitivity to tumor necrosis factor alpha is associated with respiratory defects but not with lack of cytochrome C release. *Mol Cell Biol* **27**, 1771-1783 (2007).

78 Adams, P. D. *et al.* PHENIX: a comprehensive Python-based system for macromolecular structure solution. *Acta Crystallographica Section D* **66**, 213-221, doi:doi:10.1107/S0907444909052925 (2010).

79 Rajagopal, B. S. *et al.* The hydrogen-peroxide-induced radical behaviour in human cytochrome c-phospholipid complexes: implications for the enhanced pro-apoptotic activity of the G41S mutant. *Biochem J* **456**, 441-452, doi:10.1042/BJ20130758 (2013).

80 Murshudov, G. N. *et al.* REFMAC5 for the refinement of macromolecular crystal structures. *Acta Crystallogr D Biol Crystallogr* **67**, 355-367, doi:S0907444911001314 [pii] 10.1107/S0907444911001314 (2011).

81 Joosten, R. P., Long, F., Murshudov, G. N. & Perrakis, A. The PDB_REDO server for macromolecular structure model optimization. *IUCrJ* **1**, 213-220, doi:10.1107/S2052252514009324 (2014).

82 Lee, I. *et al.* cAMP-dependent tyrosine phosphorylation of subunit I inhibits cytochrome *c* oxidase activity. *J Biol Chem* **280**, 6094-6100 (2005).

83 Pecinova, A., Drahota, Z., Nuskova, H., Pecina, P. & Houstek, J. Evaluation of basic mitochondrial functions using rat tissue homogenates. *Mitochondrion* **11**, 722-728, doi:10.1016/j.mito.2011.05.006 (2011).

84 Frezza, C., Cipolat, S. & Scorrano, L. Organelle isolation: functional mitochondria from mouse liver, muscle and cultured fibroblasts. *Nat Protoc* **2**, 287-295, doi:10.1038/nprot.2006.478 (2007).

85 Kabsch, W. Xds. *Acta Crystallogr D Biol Crystallogr* **66**, 125-132, doi:10.1107/S0907444909047337 (2010).

86 Vonrhein, C. *et al.* Data processing and analysis with the autoPROC toolbox. *Acta Crystallogr D Biol Crystallogr* **67**, 293-302, doi:10.1107/S0907444911007773 (2011).

87 Emsley, P., Lohkamp, B., Scott, W. G. & Cowtan, K. Features and development of Coot. *Acta Crystallogr D Biol Crystallogr* **66**, 486-501, doi:10.1107/S0907444910007493 (2010).

88 Winn, M. D. *et al.* Overview of the CCP4 suite and current developments. *Acta Crystallographica Section D* **67**, 235-242, doi:doi:10.1107/S0907444910045749 (2011).

89 Krieger, E. & Vriend, G. New ways to boost molecular dynamics simulations. *J Comput Chem* **36**, 996-1007, doi:10.1002/jcc.23899 (2015).

90 Duan, Y. *et al.* A point-charge force field for molecular mechanics simulations of proteins based on condensed-phase quantum mechanical calculations. *J Comput Chem* **24**, 1999-2012, doi:10.1002/jcc.10349 (2003).

91 Krieger, E., Koraimann, G. & Vriend, G. Increasing the precision of comparative models with YASARA NOVA--a self-parameterizing force field. *Proteins* **47**, 393-402 (2002).

92 Essmann, U. *et al.* A smooth particle mesh Ewald method. *J Chem Phys* **103**, 8577-8593, doi:doi:http://dx.doi.org/10.1063/1.470117 (1995).

93 Dickerson, L. in *The Gale Encyclopedia of Science* Vol. 1 (eds K.L. Lerner & B.W. Lerner) 500-502 (Gale Group, 2004).

94 Garcia-Heredia, J. M. *et al.* Tyrosine phosphorylation turns alkaline transition into a biologically relevant process and makes human cytochrome c behave as an anti-apoptotic switch. *J Biol Inorg Chem* **16**, 1155-1168, doi:10.1007/s00775-011-0804-9 (2011).

95 Cammack, R. in *Bioenergetics - A Practical Approach* (ed G.C. Brown and C.E. Cooper) 93-95 (IRL Press, 1995).

96 Kagan, V. E. *et al.* Cytochrome c/cardiolipin relations in mitochondria: a kiss of death. *Free Radic Biol Med* **46**, 1439-1453 (2009).

97 Vempati, U. D., Han, X. & Moraes, C. T. Lack of cytochrome c in mouse fibroblasts disrupts assembly/stability of respiratory complexes I and IV. *J Biol Chem* **284**, 4383-4391, doi:10.1074/jbc.M805972200 (2009).

98 Liu, S. S. Cooperation of a "reactive oxygen cycle" with the Q cycle and the proton cycle in the respiratory chain--superoxide generating and cycling mechanisms in mitochondria. *J Bioenerg Biomembr* **31**, 367-376 (1999).

99 Obenauer, J. C., Cantley, L. C. & Yaffe, M. B. Scansite 2.0: Proteome-wide prediction of cell signaling interactions using short sequence motifs. *Nucleic Acids Res* **31**, 3635-3641 (2003).

100 Zhao, X. *et al.* Phosphoproteome analysis of functional mitochondria isolated from resting human muscle reveals extensive phosphorylation of inner membrane protein complexes and enzymes. *Mol Cell Proteomics* **10**, M110 000299, doi:10.1074/mcp.M110.000299 (2011).

101 Hopper, R. K. *et al.* Mitochondrial matrix phosphoproteome: effect of extra mitochondrial calcium. *Biochemistry* **45**, 2524-2536 (2006).

102 Sanishvili, R., Volz, K. W., Westbrook, E. M. & Margoliash, E. The low ionic strength crystal structure of horse cytochrome c at 2.1 Å resolution and comparison with its high ionic strength counterpart. *Structure* **3**, 707-716 (1995).

103 Sugitani, R. & Stuchebrukhov, A. A. Molecular dynamics simulation of water in cytochrome c oxidase reveals two water exit pathways and the mechanism of transport. *Biochim Biophys Acta* **1787**, 1140-1150, doi:10.1016/j.bbabio.2009.04.004 (2009).

104 Tsukihara, T. *et al.* The low-spin heme of cytochrome c oxidase as the driving element of the proton-pumping process. *Proc Natl Acad Sci U S A* **100**, 15304-15309 (2003).

105 Zhou, M. *et al.* Atomic structure of the apoptosome: mechanism of cytochrome c- and dATP-mediated activation of Apaf-1. *Genes Dev* **29**, 2349-2361, doi:10.1101/gad.272278.115 (2015).

106 Hallows, K. R., Mount, P. F., Pastor-Soler, N. M. & Power, D. A. Role of the energy sensor AMP-activated protein kinase in renal physiology and disease. *Am J Physiol Renal Physiol* **298**, F1067-1077, doi:10.1152/ajprenal.00005.2010 (2010).

107 Zaidi, S., Hassan, M. I., Islam, A. & Ahmad, F. The role of key residues in structure, function, and stability of cytochrome-c. *Cell Mol Life Sci* **71**, 229-255, doi:10.1007/s00018-013-1341-1 (2014).

108 Guerra-Castellano, A., Diaz-Moreno, I., Velazquez-Campoy, A., De la Rosa, M. A. & Diaz-Quintana, A. Structural and functional characterization of phosphomimetic mutants of cytochrome c at threonine 28 and serine 47. *Biochim Biophys Acta*, doi:10.1016/j.bbabio.2016.01.011 (2016).

109 Hardie, D. G. AMPK-Sensing Energy while Talking to Other Signaling Pathways. *Cell Metab* **20**, 939-952, doi:10.1016/j.cmet.2014.09.013 (2014).

110 Dugan, L. L. *et al.* AMPK dysregulation promotes diabetes-related reduction of superoxide and mitochondrial function. *J Clin Invest* **123**, 4888-4899, doi:10.1172/JCI66218 (2013).

111 Ix, J. H. & Sharma, K. Mechanisms linking obesity, chronic kidney disease, and fatty liver disease: the roles of fetuin-A, adiponectin, and AMPK. *J Am Soc Nephrol* **21**, 406-412, doi:10.1681/ASN.2009080820 (2010).

112 Satriano, J., Sharma, K., Blantz, R. C. & Deng, A. Induction of AMPK activity corrects early pathophysiological alterations in the subtotal nephrectomy model of

chronic kidney disease. *Am J Physiol Renal Physiol* **305**, F727-733, doi:10.1152/ajprenal.00293.2013 (2013).

113 Tong, W. H. *et al.* The glycolytic shift in fumarate-hydratase-deficient kidney cancer lowers AMPK levels, increases anabolic propensities and lowers cellular iron levels. *Cancer Cell* **20**, 315-327, doi:10.1016/j.ccr.2011.07.018 (2011).

114 Takiyama, Y. *et al.* Tubular injury in a rat model of type 2 diabetes is prevented by metformin: a possible role of HIF-1alpha expression and oxygen metabolism. *Diabetes* **60**, 981-992, doi:10.2337/db10-0655 (2011).

115 Hüttemann, M., Lee, I., Grossman, L. I., Doan, J. W. & Sanderson, T. H. Phosphorylation of mammalian cytochrome c and cytochrome c oxidase in the regulation of cell destiny: respiration, apoptosis, and human disease. *Adv Exp Med Biol* **748**, 237-264, doi:10.1007/978-1-4614-3573-0_10 (2012).

116 Lempiainen, J., Finckenberg, P., Levijoki, J. & Mervaala, E. AMPK activator AICAR ameliorates ischaemia reperfusion injury in the rat kidney. *Br J Pharmacol* **166**, 1905-1915, doi:10.1111/j.1476-5381.2012.01895.x (2012).

ABSTRACT

REGULATION OF CYTOCHROME *c* FUNCTIONS BY PHOSPHORYLATION

by

GARGI MAHAPATRA

August 2016

Advisor: Dr. Maik Hüttemann

Major: Biochemistry and Molecular Biology

Degree: Doctor of Philosophy

Mammalian cytochrome *c* (Cytc), the only water-soluble component of the electron transfer chain plays a key role in cellular life and death decisions, functioning as an electron carrier in the electron transport chain (ETC) and as a trigger of apoptosis when released. However, its regulation is not well understood. Modified Cyt*c* purification techniques that leads to the purification of the protein maintaining the physiological phosphorylation status within the particular organ depicts a novel means of regulation via cell signaling pathways that is yet to be studied in detail. Four phosphorylation sites have been mapped on mammalian Cyt*c* till date, and two of them have been studied functionally, demonstrating that both respiration and apoptosis are under the control of signaling pathways that have yet to be identified. Our previous studies showed that Cyt*c* is phosphorylated on Tyr48 in liver, on Tyr97 in heart, and here we show that Cyt*c* is phosphorylated on Thr28 in kidneys. Our study shows that phosphorylation of Cyt*c* on Thr28 causes an inhibition of respiration in the reaction with cytochrome *c* oxidase. Thr28 is located at a central position near the heme crevice as we show here by high resolution

crystallography. Introduction of Thr28Glu phosphomimetic Cyt*c* into Cyt*c* knockout cells shows that intact cell respiration, mitochondrial membrane potential ($\Delta\Psi_m$), and ROS levels are reduced compared to wild-type. Finally, Thr28 phosphorylation is mediated by AMP kinase, which colocalizes with Cyt*c* to the intermembrane space. We conclude that Cyt*c* phosphorylation leads to regulation of ETC flux via 'controlled respiration,' preventing $\Delta\Psi_m$ hyperpolarization, a known cause of ROS and a trigger of apoptosis.

AUTOBIOGRAPHICAL STATEMENT

GARGI MAHAPATRA

2010-2016 Ph.D. in Biochemistry and Molecular Biology, Wayne State University, Detroit, MI, USA

2006-2008 M.Sc. in Biochemistry, University of Calcutta, Kolkata, India

2003-2006 B.Sc. in Physiology, University of Calcutta, Kolkata, India

HONORS AND AWARDS:

Second position, Graduate Student Research Day 2015, Wayne State University

Graduate Student Professional Travel award, Wayne State University,

Travel award sponsored by Dr. C. P. Lee, 2015, Wayne State University

Graduate Dissertation Fellowship, 2014, Wayne State University School of Medicine

National Merit Scholarship Scheme for travel assistance to USA from Kolkata, India

PROFESSIONAL MEMBERSHIPS:

American Society of Biochemistry and Molecular Biology

PUBLICATIONS:

Sanderson T. H. (CO), **Mahapatra G. (CO)**, Pecina P., Ji Q., Yu K., Sinkler C., Varughese A., Kumar R., Bukowski M. J., Tousignant R. N., Salomon A. R., Lee I., Hüttemann M. "Cytochrome C is tyrosine 97 phosphorylated by neuroprotective insulin treatment." PLoS One, 2013 8(11):e78627

Hüttemann M, Helling S, Sanderson TH, Sinkler C, Samavati L, Mahapatra G, Varughese A, Lu G, Liu J, Ramzan R, Vogt S, Grossman LI, Doan JW, Marcus K, Lee I. "Regulation of mitochondrial respiration and apoptosis through cell signaling: cytochrome c oxidase and cytochrome c in ischemia/reperfusion injury and inflammation." Biochim Biophys Acta. 2012 1817(4):598-609.